1   Type Revision 2

2   Mass transfer associated with chloritization in the hydrothermal alteration process of granitic

3   pluton.

4   Takashi Yuguchi[a,*], Takanobu Matsuki[a], Yuya Izumino[a], Eiji Sasao[b], and Tadao Nishiyama[c]

5   [a] Faculty of Science, Yamagata University, 1-4-12 Kojirakawa, Yamagata 990-8560, Japan.

6   [b] Japan Atomic Energy Agency, 1-64, Yamanouchi, Akiyo, Mizunami, Gifu 509-6132, Japan.

7   [c] Department of Earth and Environmental Science, Faculty of Advanced Science and

8   Technology, Kumamoto University, 2-39-1, Kurokami, Chuo-ku, Kumamoto 860-8555,

9   Japan.

10   * Corresponding author: T. Yuguchi

11   *E-mail address*: takashi_yuguchi@sci.kj.yamagata-u.ac.jp

12   Tel: +81 23 628 4641 / Fax: +81 23 628 4661

13

ABSTRACT

14

15   This study, along with our previous studies (Yuguchi et al., 2015; 2019A), reveals the

16   hydrothermal alteration processes in a pluton, with a focus on the mass transfer between

17   minerals and hydrothermal fluid. It also depicts the sequential variations in fluid chemistry

18   as alteration progresses. Hydrothermal alteration of the Toki granite in Tono, Japan—the

19   study area of this research—progressed through the successive processes of chloritization,

20   plagioclase alteration, and precipitation of a carbonate mineral [biotite chloritization

21   described by Yuguchi et al. (2015) and plagioclase alteration by Yuguchi et al. (2019A)]. This

22   paper describes the alteration process of hornblende chloritization, K-feldspar chloritization,

23   and the formation of fracture-filling chlorite through petrography and mineral chemistry. A

24   set of singular value decomposition analyses was conducted to obtain reaction equations for

25   the chloritization processes, which facilitates the quantitative assessment of mass transfer

26   between the reactant and product minerals, and the inflow and outflow of components

27   through the hydrothermal fluid. Hornblende chloritization is accompanied by mass transfer

28   with an inflow of Al^{3+}, Fe^{2+}, Mn^{2+}, and Mg^{2+} and an outflow of Ca^{2+}, K^+, Na^+, and H^+. Mass

29   transfer of K-feldspar chloritization is essentially characterized by an inflow of Al^{3+}, Fe^{2+},

30   and Mg^{2+} and an outflow of H_4SiO_4, K^+, and H^+ into the hydrothermal fluid. Several types

31   of chloritization reactions (including biotite chloritization) can be characterized by their

32   reaction with the inflow of Al^{3+}, Fe^{2+}, Mn^{2+}, and Mg^{2+} and the outflow of H_4SiO_4, Ca^{2+}, K^+,

33   and F^-.

34   The age and thermal conditions of hornblende chloritization (64–54 Ma and 330–190°C),

35   K-feldspar chloritization (68–53 Ma and 350–210°C), and precipitation of fracture-filling

36   chlorite (66 and 63 Ma, 340 and 320°C) are overlapped with those of biotite chloritization

37   (68–51 Ma and 350–180°C). The reactions of chloritization (this study and Yuguchi et al.,

38   2015) and plagioclase alteration (Yuguchi et al., 2019A) represent the sequential variations

39   in fluid chemistry at temporal conditions from 68 Ma to 51 Ma as the temperature decreased

40   from 350°C to 180°C. As the alteration proceeds, the concentrations of aluminum, iron,

41   manganese, and magnesium ions in the hydrothermal fluid decrease gradually, and those of

42   calcium, hydrogen, and fluorine ions increase gradually.

43   Hornblende chloritization associates with formation of magnetite and ilmenite. The

44   thermal conditions of the hydrothermal fluid yielding the formation of magnetite and ilmenite

45   can be interpreted by the chemical characteristics of chlorite around their associated minerals.

46   The formation temperature of magnetite was higher than that of ilmenite, implying a decrease

47   in oxygen fugacity in the hydrothermal fluid with the decrease in temperature from 280–

48   310°C to 220–250°C.

49   Keywords: Hydrothermal alteration; chloritization; dissolution and precipitation; mass

50   transfer; singular value decomposition (SVD) analysis.

51

INTRODUCTION

52

53 This study focuses on 1) the nature of the chloritization reaction and mass transfer due to

54 hydrothermal alteration in a granitic pluton, based on petrography and mineral chemistry, 2)

55 the physical conditions, including timing and temperature of alteration, and 3) the evolution

56 of fluid chemistry as the alteration progresses, with the Toki granite in Tono district, central

57 Japan, as an example. The degree and extent of hydrothermal alteration within a granitic body

58 have a significant effect on the subsequent weathering of the granitic rock. It also influences

59 the chemical characteristics of the palaeogroundwater and present-day groundwater due to

60 water–rock interactions. Predicting geochemical behavior, evolution, and water–rock

61 interaction is important to the safety assessment for long-term geological disposal of nuclear

62 waste and underground storage of oil, natural gas, and hydrogen (e.g. Carpenter et al., 2017).

63 For example, it allows us to predict whether oxidative fluid (groundwater) will cause the

64 corrosion of artificial metal objects in the facilities (Yuguchi et al., 2019A).

65 The hydrothermal alteration of granitic rock is constrained mainly by the dissolution–

66 precipitation processes during the penetration of hydrothermal fluid along the microcracks

67 (Nishimoto and Yoshida, 2010; Yuguchi et al., 2015). The alteration is also influenced by the

68 mass transfer of chemical components due to rock–matrix diffusion and through the

69 micropore network (Alexander et al., 2009; Neretnieks, 2017; Yuguchi et al., 2019A).

70 The hydrothermal alteration of the Toki granite progresses through the following

71 successive processes: 1) chloritization, 2) plagioclase alteration consisting of albitization, K-

72 feldspathization, illitization, epidotization, smectitization, and formation of fluorite, and 3)

73 precipitation of carbonate mineral (Nishimoto et al., 2008). Four processes occur during Toki

4

74 granite chloritization: biotite chloritization (Yuguchi et al., 2015), hornblende chloritization,

75 K-feldspar chloritization, and fracture-filling chlorite formation (see petrography). Chlorites

76 of hydrothermal origin in granitic rocks hold records of the hydrothermal fluid chemical

77 characteristics (Yuguchi et al., 2015). This study describes the petrography and chemistry of

78 the hornblende chloritization, K-feldspar chloritization, and fracture-filling chlorite

79 precipitation, which enable us to further discuss the nature of alteration reactions and mass

80 transfer due to hydrothermal fluid advection in granitic pluton, and the alteration

81 temperatures leading to chloritization. Furthermore, a combination of this study and Yuguchi

82 et al. (2015) provides a comprehensive characterization of the mass transfer of the overall

83 chloritization and the sequential variation in fluid chemistry in the cooling pluton.

84 Plagioclase alteration is closely related to chloritization in the Toki granite (Yuguchi et

85 al., 2019A). The mass transfer and physical conditions (age and temperature) of plagioclase

86 alteration in the Toki granite have already been reported by Yuguchi et al. (2019A). Mass

87 transfer through the overall chloritization process and the plagioclase alteration process

88 provides significant clues regarding the nature of the sequential and long-term variations in

89 fluid chemistry in a granitic pluton across a wide temperature range during sub-solidus

90 cooling.

91 The Toki granite has two 500-m long vertical shafts (see Sampling and Analytical

92 Procedures) that enables us to extract deep drill core samples from within the pluton. These

93 samples have escaped weathering, and thus are suitable for the study of chloritization. The

94 time–temperature (t–T) path of the sampling site, obtained by Yuguchi et al. (2019B), is also

95 applicable to the study and can simultaneously yield both the age and temperature of the

96   secondary minerals (Yuguchi et al., 2019B). The chemical composition of the chlorite reveals

97   the formation temperature through a chlorite geothermometer (e.g., empirical thermometer

98   of Yoneda and Maeda, 2008), and subsequently, this formation temperature provides the

99   corresponding age through examination of the t–T path. Therefore, both the age and

100   temperature of the chloritization can be determined, enabling us to discuss the sequential

101   variations in the fluid chemistry.

102

THE TOKI GRANITE

103

104   In the inner zone (northern side of the Median Tectonic Line) of the Southwest Japan Arc,

105   the late Cretaceous granitic rocks are widely distributed in parallel, east–west oriented Ryoke,

106   Sanyo, and San-in Belts (Ishihara, 2003). The Toki granite in the Tono district of central

107   Japan is one of the Late Cretaceous plutonic bodies of the Sanyo Belt (Fig. 1A: Ishihara and

108   Chappell, 2007). The Toki granite is a stock of about 14×12 km^2 (Ishihara and Suzuki, 1969)

109   that intrudes into the Jurassic sedimentary rocks of the Kamiaso unit in Mino Terrane (Sano

110   et al., 1992), as well as the Late Cretaceous Nohi rhyolite (Sonehara and Harayama, 2007)

111   (Fig. 1B). The Toki granite is overlain unconformably by the Miocene Mizunami Group and

112   the Mio-Pleistocene Tokai Group (Itoigawa, 1974; 1980; Todo Collaborative Research Group,

113   1999).

114   The Toki granite has a whole-rock Rb–Sr isochron age of 72.3 ± 3.9 Ma (Shibata and

115   Ishihara, 1979), a monazite chemical Th-U-total Pb isochron (CHIME) age of 68.3 ± 1.8 Ma

116   (Suzuki and Adachi, 1998), zircon U–Pb ages of 74.7 ± 4.2 to 70.4 ± 1.7 Ma (Yuguchi et al.,

117   2016), a hornblende K–Ar age of 74.3 ± 3.7 Ma (Yuguchi et al., 2011A), biotite K–Ar ages

118   of 78.5 ± 3.9 to 59.7 ± 1.5 Ma (N = 33: Yuguchi et al., 2011A), zircon fission-track (ZFT)

119   ages of 75.6 ± 3.3 to 52.8 ± 2.6 Ma (N = 44: Yuguchi et al., 2011A), and apatite fission-track

120   (AFT) ages ranging from 52.1 ± 2.8 to 37.1 ± 3.6 Ma (N = 33: Yuguchi et al., 2017). Based

121   on the phase relationships, Yamasaki and Umeda (2012) estimated that the emplacement

122   depth of granitic magma was about 5–7 km below the surface.

123   A series of studies by the authors describes the formation history of the Toki granitic

124   pluton from intrusion through emplacement to cooling (Yuguchi et al., 2010; 2011A; 2011B;

125   2011C; 2013; 2015; 2016; 2017; 2019B). The Toki granite, a zoned pluton, has three rock

126   facies grading from muscovite-biotite granite (MBG) at the margin through hornblende-

127   biotite granite (HBG) to biotite granite (BG) in the interior (Fig. 1C). The geology and

128   petrography of the Toki granite were described in detail in Yuguchi et al., (2010, 2011B;

129   2011C). A description of the hydrothermal alteration in the Toki granite was given in

130   Nishimoto et al. (2008), Nishimoto and Yoshida (2010), Ishibashi et al. (2014), Yuguchi et al.

131   (2015), Ishibashi et al. (2016), and Yuguchi et al. (2019A).

132

133   **SAMPLING AND ANALYTICAL PROCEDURES**

134   The Mizunami Underground Research Laboratory, which consists of two vertical shafts (the

135   main and ventilation shafts), is located on the sedimentary Mizunami Group, which

136   unconformably overlies the Toki granite (Fig. 1B, D, and E). The main and ventilation shafts

137   are 500-m deep, ranging from an altitude of 201 masl (meters above sea level) (ground level)

138   to an altitude of -299 masl (shaft bottom) (Fig. 1E). The unconformity between the Mizunami

139   Group and the Toki granite is intersected by the shafts at a depth of about 170 m. This study

140   employed borehole 06MI03 (vertical and 336-m long). The borehole 06MI03 was drilled

141   from a depth of 191 m in the ventilation shaft before continuing the excavation below 191 m

142   (Fig. 1E). Yuguchi et al. (2015) and Yuguchi et al. (2019A) describe the petrography and

143   mineral chemistry of biotite chloritization and plagioclase alteration, respectively, in rock

144   samples collected from the rock mass at a depth of approximately 500 m (-299 masl) in the

145   ventilation shaft (Fig. 1E). This study employed the same samples originating from the

146   deepest section of borehole 06MI03 in the depth range of -274 to -314 masl (9 samples spaced

147   5 m apart) (Fig. 1E). This restricted sampling interval provides rock samples of the same

148   temperature and pressure history in the sub-solidus cooling process of the Toki granite.

149   The petrographical data in this study were obtained from two-dimensional thin sections.

150   The thin sections were prepared carefully in order to prevent the detachment of minerals.

151   Backscattered electron (BSE) images and chemical maps were generated using a JEOL

152   IT100A scanning electron microscope with an energy-dispersive X-ray spectrometer (EDS),

153   at Yamagata University, operating at an accelerating voltage of 15 kV and a beam current of

154   1.5 nA. Mineral compositions were analyzed using an electron microprobe analyzer (JEOL

155   JXA-8900) with a wavelength-dispersive X-ray spectrometer (WDS), at Yamagata

156   University. The analytical conditions required by the quantitative analysis were an

157   acceleration voltage of 15 kV, a beam current of 20 nA, a beam diameter of 3 μm, and the

158   ZAF data correction method. The area (pixel area) of the minerals and microvoids (and

159   microcracks) were determined using Photoshop® image processing software. Details of the

160   analysis procedure are described in Appendix A.

161

162   **PETROGRAPHY**

163   **Hornblende chloritization**

164   Hornblende chloritization represents chlorite partially replacing hornblende, as shown in Fig.

165   2. The distributions of hornblende and chlorite in the altered grain are shown by elemental

166   silicon and calcium maps in Fig. S1. Hornblende exhibits composition from ferroedenite to

167   ferropargasite (Table S1). Chloritization proceeds from the rim to the core in hornblende

168   along its cleavage, and the micrometer-scale voids (hereinafter referred to as 'microvoid')

169   occur between reactant hornblende and product chlorite (Fig. 2A-3 and A-4). Such

170   microvoids and deformation texture of hornblende indicate the decrease in volume from the

171   reactant to the product in the chloritization reaction. Biotite chloritization, however, does not

172   exhibit microvoids between the reactant biotite and the product chlorite, in the sample with

173   occurrences of hornblende chloritization and biotite chloritization (e.g., Fig. 6 of Yuguchi et

174   al., 2015). In thin section, the difference in microvoid frequency between the hornblende and

175   biotite chloritizations indicates that microvoid production is not attributed to mineral

176   detachment during thin-section preparation. In the hornblende chloritization, the microvoids

177   contain small isolated fragments of hornblende. The surfaces of small fragments are flat and

178   smooth (refer to Fig. S2). If the fragment was caused by hornblende detachment due to

179   polishing during preparation, the surfaces would not necessarily be flat and smooth. This is

180   also an evidence that the hornblende fragments were not caused by the detachment during

181   preparation. The chlorite composition ranges from 5.40–6.16 atoms per formula unit (apfu)

182   in Si (mean: 5.64 apfu, N = 58), with an almost constant $Fe / (Fe + Mg)$ of 0.71–0.79. Chlorite

183   is associated with minerals such as titanite, epidote, albite, K-feldspar, ilmenite, magnetite,

184   quartz, fluorite, and calcite, which are all products of chloritization. Hornblende

185   chloritization is further subdivided into the following five subtypes by the assemblage of

186   product minerals (Table 1; Figs. 2, S2, S3, and S4):

187   Sample No. 3-2-9: chlorite, albite, K-feldspar, illite, and magnetite products (Fig. 2 and S1)

188   Sample No. 3-6: chlorite, titanite, epidote, quartz, and calcite products (Fig. S2)

189   Sample No. 7-8: chlorite, titanite, and albite products (Fig. 2)

190   Sample No. 10-1: chlorite, titanite, and quartz products (Fig. S3)

191   Sample No. 10-4: chlorite, titanite, epidote, fluorite, quartz, and calcite products (Fig. S4)

192   Titanite—identified by elemental titanium mapping—occurs as lenticular or bead-like

193   grains, veinlets (>10 μm width: Fig. S2), and irregular grains (>5 μm across: Figs. S3 and

194   S4) inside the chlorite. Similarly, epidote occurs as lenticular and bead-like grains (>5 μm

195   wide: sample No. 3–6 of Fig. S2) and rounded grains (>100 μm across: sample No. 10–4 of

196   Fig. S4). Albite occurs as rounded grains and K-feldspar occurs as lenticular, bead-like, and

197   irregular grains (Fig. 2). Ilmenite (>25 μm wide) occurs as lenticular and bead-like grains in

198   chlorite, and its elongations are oriented parallel to the hornblende cleavage (Fig. 2A-3).

199   Rounded magnetite (sizes of up to 20 μm) occurs in chlorite (Fig. 2A-4). Magma-origin

200   plagioclase has compositions ranging from Ab_{70} to Ab_{82} (Yuguchi et al., 2010). Hydrothermal

201   albite in hornblende chloritization has a composition with $> Ab_{90}$ (Table S1), which is

202   consistent with hydrothermal albite accompanying plagioclase alteration ($> Ab_{90}$: Yuguchi et

203   al., 2019A). The chemical compositions are not substantially different between hydrothermal

204   K-feldspar and ilmenite (Table S1) and magma-origin K-feldspar and ilmenite (Tables 3 and

205   4 of Yuguchi et al., 2010). Although the chemistries are the same, whether they have

206   hydrothermal or magmatic origin can be identified by their petrographical occurrences;

207   hydrothermal albite, K-feldspar, and ilmenite occur at the boundary between hornblende and

208   chlorite or occur as inclusions within chlorite. Hydrothermal magnetite contains more MnO

209   and MgO components than magmatic magnetite (Table S1 and Table 4 of Yuguchi et al.,

210   2010). Granular quartz, fluorite, and calcite with sizes of up to 20 μm are observed in the

211   hornblende chloritization; quartz is identified by silicon maps of Figs. S2C, S3E, and S4D,

212   and fluorite and calcite are identified by calcium maps of Figs. S2C and S4D. In sample No.

213   3-6, the calcite is included in chlorite (Fig. S2). Such an occurrence implies that calcite

214   formation accompanies hornblende chloritization.

215   **K-feldspar chloritization**

216   K-feldspar chloritization represents the occurrence of chlorite partially replacing K-feldspar,

217   as shown in Fig. 3A. The distributions of K-feldspar and chlorite are illustrated by elemental

218   silicon, iron, magnesium, and potassium maps in Fig. S5. K-feldspar is often accompanied

219   by perthitic textures (Fig. 3A-3). K-feldspar compositions range from Or_{90} to Or_{100} (Table

220   S1). Chlorite fragments up to 20 μm across are distributed within the K-feldspar parts in

221   contact with chlorite. Although the hornblende chloritization has microvoids between the

222   reactant and the products, the K-feldspar chloritization does not. No deformation texture is

223   observed within the chloritized grains (Fig. 3A), indicating solid volume conservation from

224   reactant K-feldspar to chloritization products. Chlorite composition ranges from 5.33–6.06

225   apfu in silicon (mean: 5.64 apfu, N = 29), with an almost constant Fe / (Fe + Mg) of 0.73–

226   0.82. Chlorite is essentially associated with titanite (sample No. 3-6: Table 1; Fig. 3A-4 and

227   S5). The distribution of titanite, illustrated by elemental titanium maps (Fig. S5), shows that

228   it occurs as tiny grains (up to 5 μm) inside the chlorite.

229   **Fracture-filling chlorite**

230   Fracture-filling chlorite occurs in veinlets with a few micrometers wide, and there is an

231   irregular boundary between the fracture-filling minerals and the original magmatic minerals.

232   Fracture-filling chlorite frequently connects with the altered biotite along the microfracture

233   network and grain boundary. Figure 3B shows fracture-filling chlorite with the largest

234   thickness ranging from 30–100 μm (sample No. 8-1). The chemical composition of this

235   chlorite was determined by electron probe microanalysis (EPMA). The compositions are 5.39

236   and 5.44 apfu in Si (N = 2), with an almost constant Fe / (Fe + Mg) of 0.75–0.78. Chlorite is

237   essentially associated with titanite and K-feldspar (Table 1; Fig. 3B-3 and 3B-4). The

238   distributions of chlorite, titanite, and K-feldspar are identified by the elemental maps of Fig.

239   S6: chlorite (iron map), titanite (titanium and calcium maps), and K-feldspar (potassium map).

240

DISCUSSION

Volume changes from reactant to products

241
242
243 Chlorites have consistent composition ranges among the biotite chloritization, hornblende

244 chloritization, K-feldspar chloritization, and fracture-filling processes: Mg# (Mg / (Fe + Mn

245 + Mg) in apfu) ranging from 0.17–0.29 and Si in a range of 5.33–6.20 apfu (Fig. 4). However,

246 the hornblende chloritization reaction shows a unique formation of microvoids and

247 deformation texture, which imply a decrease in volume from the reactant to the products. The

248 area (pixel area) of the reactant, products, and microvoids (and microcracks) in the chloritized

249 hornblende were determined through image analysis of the samples No. 3-2-9, 3-6, 7-8, 10-

250 1, and 10-4. The volume of the microvoids was estimated from their area, by simply assuming

251 the area–volume equivalence (Yuguchi and Nishiyama 2008), that is, the area of the

252 consumed (original) hornblende as a reactant equals the areal sum of products and microvoids.

253 The image analyses showed a 6–12% decrease in volume from the reactant to the products

254 (Table 1). No microvoids were observed in this biotite and K-feldspar chloritization process,

255 indicating solid volume conservation between reactant and products (Table 1).

Chloritization reactions

257 The chloritization process consists of biotite chloritization, hornblende chloritization, K-

258 feldspar chloritization, and fracture-filling chlorite formation. The biotite chloritization

259 reactions—satisfying both the assemblage of product minerals and the volume relationship

260 between the reactant and products—were previously studied based on the singular value

261 decomposition (SVD) analysis (Yuguchi et al., 2015). This study presents the overall

262 chemical reaction equations for hornblende and K-feldspar chloritization. From these

15

263   equations, the quantitative mass transfer between reactant and product minerals, and the

264   inflow and outflow of components with chloritization are derived. The chemical reaction for

265   producing the fracture-filling chlorite could not be established due to the lack of a reactant.

266   **Hornblende chloritization reactions.** The overall reaction equations are constructed for

267   each sample, from Nos. 3-2-9, 3-6, 7-8, 10-1, to 10-4, in hornblende chloritization. To

268   determine alteration reactions in such an open system, we must specify some conservation

269   conditions. We considered the process involving the decrease in volume from the reactants

270   to the products as a conservation process: about 12% (sample No. 3-2-9), 11% (No. 3-6), 6%

271   (No. 7-8), 12% (No. 10-1), and 11% (No. 10-4). We considered the additional condition of

272   volume ratios of the product minerals in the alteration area, to derive the reaction equations

273   (Table 1). Thus, the alteration reactions that satisfied both the volume relationship between

274   the reactants and products and the volume ratios of the product minerals were developed.

275   In the formation of the overall reaction of sample No. 3-2-9, the reactant is hornblende

276   (analysis No. E3-2-3 in Table S1; the analysis number corresponds to the location shown in

277   Fig. 2A) and the products are chlorite (No. C3-16), albite (No. E3-2-5), K-feldspar (No. E3-

278   2-6), ilmenite (No. C3-12), and magnetite (No. C3-15). The molar volumes of the reactant

279   and product minerals were derived from their chemical compositions (Table S1). The volume

280   fractions of the product minerals are expressed as ratios, such as chlorite to albite to K-

281   feldspar to ilmenite to magnetite = 1: 0.056: 0.056: 0.131: 0.002 (Table 1). Details of the

282   image analysis procedure giving the mineral ratio are described in Appendix A. We

283   considered the following reaction in an open system:

284   Hb + X = a Chl + b Ab + c Kfs + d Il + e Mag + Y (X and Y: open components), where X

285 denotes the influx of chemical components through an intergranular medium (hydrothermal

286 fluid) and Y denotes the efflux from the system. Silicon species occur in the form of H_4SiO_4

287 in the reaction equation. The solution of a set of simultaneous equations was used to

288 determine the stoichiometric coefficients, *a, b, c, d,* and *e*, and those of the open components

289 involved in X and Y. The simultaneous equations consisted of conservations (1), (2), (3), (4),

290 and (5):

291 $267.13 \times 0.88 = 212.08\ a + 100.45\ b + 108.74\ c + 32.61\ d + 41.74\ e$ (volume decrease of

292 12% from reactant to products)…conservation (1)

293 $b = 0.1176\ a$ (volume relation between chlorite and albite: $1:0.056 = 212.08a: 100.45b$)

294 …conservation (2)

295 $c = 0.1087\ a$ (volume relation between chlorite and K-feldspar: $1:0.056 = 212.08a: 108.45c$)

296 …conservation (3)

297 $d = 0.8500\ a$ (volume relation between chlorite and ilmenite: $1:0.131 = 212.08a: 32.61d$)

298 …conservation (4)

299 $e = 0.0086\ a$ (volume relation between chlorite and magnetite: $1:0.002 = 212.08a: 41.74e$)

300 …conservation (5)

301   The numerical values in conservation Equation (1) denotes molar volumes in each

302 mineral (see footnote of Table S1). Conservations (1)–(5) give the following equation:

303 $Hb + 0.495Ti^+ + 2.711Al^{3+} + 2.552Fe^{2+} + 0.265Mn^{2+} + 1.116Mg^{2+} + 0.200K^+ + 7.878H_2O$

304 $\rightarrow 0.895Chl + 0.105Ab + 0.097Kfs + 0.761Il + 0.008Mag + 0.472H_4SiO_4 + 1.685Ca^{2+} +$

305 $0.500Na^+ + 0.131F^- + 0.016Cl^- + 13.870H^+$ …reaction (A1) (Table 2)

306   The same procedures are applied to sample Nos. 3-6, 7-8, 10-1, and 10-4, to establish

307   the hornblende chloritization reaction equations, which are listed in Table 2 and described
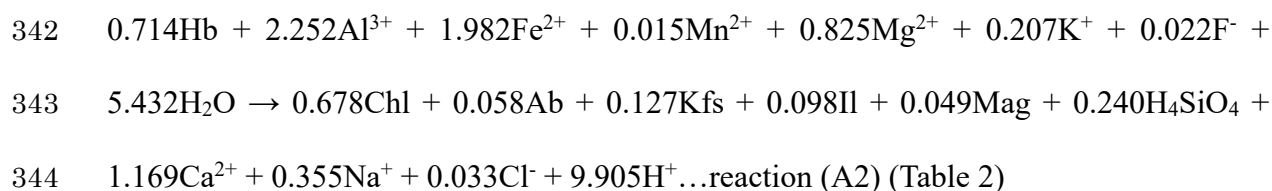
308   in Appendix B.

309   We also studied the reactions based on singular value decomposition (SVD) analysis

310   (e.g. Fisher, 1989; 1993) to establish the hornblende chloritization reactions of sample Nos.

311   3-2-9, 3-6, 7-8, 10-1, and 10-4. The SVD analysis provides a simple yet powerful tool for

312   determining univariant reactions in multicomponent mineral assemblages without

313   considering T, P, fO_2, and pH constraints (Fisher, 1989; 1993). The SVD analysis is closely

314   related to the least square method, which enables the determination of the precise mass

315   balance relationships in multicomponent mineral assemblages based on mineral analyses

316   with possible analytical errors (Fisher, 1989). The SVD analysis can also be used to analyze

317   open-system changes (Shigeno et al., 2012). In our previous study, we applied the SVD

318   analysis to model the possible reaction relationships satisfying both the assemblage of

319   product minerals and the volume relationship between reactant and products (solid volume

320   constant) in the biotite chloritization (Yuguchi et al., 2015). Thus, the SVD analysis can be

321   applied to study hornblende and K-feldspar chloritization. To determine chloritization

322   reactions in an open system, we also have to specify some conservation conditions for the

323   SVD analysis. We defined the volume constraint as a conservation condition, and assumed

324   one or more additional condition(s) of closure components among nine components (Si, Ti,

325   Al, Fe, Mn, Mg, Ca, Na, and K), for deriving the reaction relation. The matrices for SVD

326   consist of arbitrary combinations of molar volume and closure component(s) in the reactant

327   and products (Table S2). The composition matrix of the closure components is expressed in

328   terms of atoms of element per formula unit for the mineral. The free software program

329   Scilab (Scilab Enterprises S.A.S) was employed to perform the SVD analysis. The most

330   reasonable reaction among the possible reaction relationships was identified according to

331   1) the signs of stoichiometric coefficients of reactants (minus) and products (plus), and 2)

332   the least difference from the volume fraction of product minerals in the observation (Table

333   1).

334   In the formation of the overall reaction of sample No. 3-2-9 in the SVD analysis, we

335   consider a reaction in an open system as follows:

336   a Hb + X = b Chl + c Ab + d Kfs + e Il + f Mag + Y (X and Y: open components)
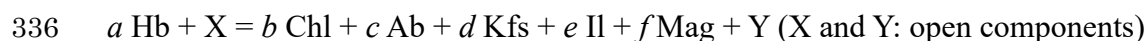
337   The SVD analysis determines stoichiometric coefficients $a, b, c, d, e,$ and f, and those

338   of open components involved in X and Y. Some matrices consisting of arbitrary

339   combinations of molar volume and closure components give several possible reactions. The

340   SVD analysis consisting two matrices of molar volume and Ti component (Table S2) gives

341   the most reasonable reaction among several possible reactions, as follows:

342    $0.714Hb + 2.252Al^{3+} + 1.982Fe^{2+} + 0.015Mn^{2+} + 0.825Mg^{2+} + 0.207K^+ + 0.022F^- +$

343    $5.432H_2O \rightarrow 0.678Chl + 0.058Ab + 0.127Kfs + 0.098Il + 0.049Mag + 0.240H_4SiO_4 +$

344    $1.169Ca^{2+} + 0.355Na^+ + 0.033Cl^- + 9.905H^+$…reaction (A2) (Table 2)

345   The reaction gives the volume fraction (proportion) of the product minerals; chlorite:

346   albite: K-feldspar: ilmenite: magnetite = 1: 0.040: 0.096: 0.022: 0.014 (Table 2). Table 2

347   shows the reasonable reaction equations in sample Nos. 3-2-9, 3-6, 7-8, 10-1, and 10-4 on

348   the basis of each matrix (Table S2) for the SVD analysis, leading to hornblende chloritization.

349   Reactions (A1) and (A2) of sample No. 3-2-9 show the production of chlorite, albite,

350   K-feldspar, ilmenite, and magnetite by consuming hornblende with an inflow of Ti^+, Al^{3+},

351   Fe^{2+}, Mn^{2+}, Mg^{2+}, K^+, F^- (reaction A2), and H_2O from the hydrothermal fluid, accompanied

352   by an outflow of H_4SiO_4, Ca^{2+}, Na^+, F^- (reaction A1), Cl^-, and H^+ into the fluid (Table 2).

353   The hornblende chloritization reactions in the SVD analyses, and the given characteristics

354   of mass transfer among the reactant, products, and hydrothermal fluid for sample Nos. 3-6,

355   7-8, 10-1, and 10-4 are described in Appendix B.

356   **K-feldspar chloritization reactions.**   The essential reaction equation was constructed for

357   the K-feldspar chloritization as an example of sample No. 3-16. The chloritization has K-

358   feldspar (No. E3-5) as the reactant, and chlorite (No. A042) and titanite (No. E3-9) as

359   products (Table S1). To determine chloritization reactions in an open system, we must

360   specify some conservation conditions. No microvoids or deformation structures were

361   observed after K-feldspar chloritization, indicating the constant solid volume between the

362   reactant and the products as a conservation condition (Table 1). Additional conservations

363   include the volume ratios of product minerals; Chl:Ttn = 1:0.070 (Table 1). The reaction

364   equation that satisfies both the volume relationship between the reactants and the products,

365   and the volume ratios of the product minerals were constructed as follows: $Kfs + 0.107Ti^+$

366    $+ 1.644Al^{3+} + 3.255Fe^{2+} + 0.203Mn^{2+} + 0.818Mg^{2+} + 0.113Ca^{2+} + 0.016F^- + 0.009Cl^- +$

367    $7.150H_2O \rightarrow 0.478Chl + 0.125Ttn + 0.287H_4SiO_4 + 0.016Na^+ + 0.911K^+ +$

368    $13.152H^+$…reaction (B1) (Table 2).

369   The SVD analysis of the matrix consisting of a conservation constraint of molar volume for

370   the three phases (Table S2) gives the most reasonable reaction relation: $0.895Kfs + 0.051Ti^+$

371    $+ 1.546Al^{3+} + 3.010Fe^{2+} + 0.188Mn^{2+} + 0.756Mg^{2+} + 0.050Ca^{2+} + 0.007F^- + 0.009Cl^- +$

372    $6.456H_2O \rightarrow 0.443Chl + 0.055Ttn + 0.236H_4SiO_4 + 0.014Na^+ + 0.814K^+ +$

20

373   11.968H^+…reaction (B2) (Table 2)

374   The reaction equation gives the volume fraction of the product minerals; chlorite to

375   titanite = 1: 0.033 (Table 2). Both reactions (B1) and (B2) represent the chloritization, and

376   the production of titanite by the consumption of K-feldspar, with an inflow of Ti^+, Al^{3+}, Fe^{2+},

377   Mn^{2+}, Mg^{2+}, Ca^{2+}, F^-, Cl^-, and H_2O from the hydrothermal fluid, accompanied by the

378   outflow of H_4SiO_4, Na^+, K^+, and H^+ into the hydrothermal fluid (Table 2).

379   **Characteristics of mass transfer leading to chloritization**

380   **Mass transfer leading to biotite chloritization.**   Biotite chloritization occurs with high

381   frequency among all chloritization processes. It involves two formation mechanisms: 1)

382   solid volume replacement from the reactant biotite to the chloritization products, and 2) the

383   dissolution of biotite and the precipitation of chloritization products (Ishii et al., 2017).

384   Characteristics of mass transfer leading to biotite chloritization are described in Yuguchi et

385   al. (2015) in detail. Biotite chloritization is characterized by essential mass transfer: inflow

386   of Al^{3+}, Fe^{2+}, Mn^{2+} Ca^{2+}, and H^+ from the hydrothermal fluid and outflow of H_4SiO_4 (Si^{4+}),

387   K^+ and F^- into the hydrothermal fluid (Fig. 5).

388   **Mass transfer leading to hornblende chloritization.**   Hornblende chloritization was

389   derived from the dissolution of hornblende and the precipitation of chlorite and associated

390   minerals, which is characterized by the following features: inflow of Al^{3+}, Fe^{2+}, Mn^{2+}, and

391   Mg^{2+} and outflow of Ca^{2+}, K^+, Na^+, and H^+ (Table 2; Fig. 5). Titanium derived from

392   hornblende and inflow of Ti^+ from the hydrothermal fluid produce the formation of ilmenite

393   or titanite, while hornblende-derived titanium is released into the hydrothermal fluid for small

394   quantities of ilmenite or titanite (Table 2). Calcium derived from hornblende produces

21

395   calcium-bearing minerals such as titanite, epidote, fluorite, and calcite, and the rest is released

396   into the hydrothermal fluid (Table 2). The inflow of CO_2 from the hydrothermal fluid results

397   in calcite production. Hydrogen ions are observed as a product (right-hand side) in the overall

398   reactions (Table 2). Therefore, the H^+ concentration of the hydrothermal fluid gradually

399   increases as the plagioclase alteration proceeds, indicating a gradual decrease in potential of

400   hydrogen (pH) in the hydrothermal fluid.

401   **Mass transfer leading to K-feldspar chloritization.**   K-feldspar chloritization is caused

402   by the dissolution of K-feldspar and the precipitation of chlorite and titanite. K-feldspar

403   chloritization is essentially characterized by the decomposition of K-feldspar with an inflow

404   of Al^{3+}, Fe^{2+}, and Mg^{2+} and an outflow of H_4SiO_4, K^+, and H^+ into the hydrothermal fluid

405   (Table 2). Hydrogen ions are observed as products (right-hand side) in the chloritization

406   reactions (Table 2), indicating a gradual increase in the H^+ concentration of the

407   hydrothermal fluid as the plagioclase alteration proceeds, i.e. a gradual decrease in pH of

408   the hydrothermal fluid.

409   **Mass transfer leading to the formation of fracture-filling chlorite.**   The formation of

410   fracture-filling chlorite is due to the precipitation of chlorite, titanite, and K-feldspar, which

411   is characterized by the inflow of H_4SiO_4, Ti^+, Al^{3+}, Fe^{2+}, Mn^{2+}, Mg^{2+}, Ca^{2+}, Na^+, K^+, F^-, and

412   Cl^- from the hydrothermal fluid. All components constituting chlorite, titanite, and K-

413   feldspar are supplied by the hydrothermal fluid.

414   **Thermal and temporal relationships among all chloritizations**

415   **Temperature conditions in all chloritizations**.   Chlorite geothermometers have been

416   proposed based on compositional variability (De Caritat et al., 1993) including: 1) an

22

417 empirical thermometer based on tetrahedral aluminum occupancy as a function of

418 temperature (e.g., Cathelineau and Nieva, 1985; Cathelineau, 1988; Kranidiotis and

419 MacLean, 1987; Jowett, 1991; Yoneda and Maeda, 2008) and 2) a thermodynamic

420 thermometer based on equilibrium between chlorite and aqueous solution (solid solution

421 model) (e.g. Walshe, 1988; Vidal et al., 2001; Inoue et al., 2009; 2010, 2018). Both empirical

422 and thermodynamic studies indicate that tetrahedral aluminum in chlorite is a temperature-

423 dependent parameter. The variation in not only in the tetrahedral aluminum but also that the

424 Fe / (Fe + Mg) in chlorite should be considered in the determination of the formation

425 temperature (Bourdelle et al., 2013).

426   In the Toki granite, chlorite compositions show that tetrahedral aluminum values range

427 from 1.70–2.67 apfu (mean value of 2.31 apfu, N = 143) in biotite-origin chlorite (Yuguchi

428 et al., 2015), from 1.84–2.60 apfu (mean value of 2.36 apfu, N = 57) in hornblende-origin

429 chlorite, from 1.94–2.67 apfu (mean value of 2.38 apfu, N = 28) in K-feldspar-origin chlorite,

430 and are 2.56 and 2.61 apfu (N = 2) in fracture-filling chlorite (Fig. 6A). The Fe / (Fe + Mg)

431 range is from 0.82–0.92 (mean value of 0.86) in biotite-origin chlorite (Yuguchi et al., 2015),

432 0.80–0.91 (mean value of 0.85) in hornblende-origin chlorite, 0.85–0.92 (mean value of 0.89)

433 in K-feldspar-origin chlorite, and are 0.84 and 0.87 in fracture-filling chlorite (Table S1).

434 There is no correlation between tetrahedral aluminum and Fe / (Fe + Mg). The above

435 chemical observation indicates that the tetrahedral aluminum in chlorites can be used to show

436 at least the relative difference in chloritization temperature conditions among all

437 chloritization processes.

438   A rough temperature index was estimated using the chlorite geothermometer by Yoneda

23

439   and Maeda (2008), on the assumption that the equilibrium among minerals and hydrothermal

440   fluid is established (Fig. 6B). This geothermometer was employed for estimating the

441   temperature for the biotite chloritization in the study of Yuguchi et al. (2015). All the

442   chloritization processes have temperature intervals between about 350°C and 180°C. Such

443   temperature intervals indicate the chloritization stage in the sub-solidus cooling process of

444   the Toki granite (Fig. 6B). The biotite, hornblende, and K-feldspar chloritization processes

445   have temperature conditions from 350–180°C (Yuguchi et al., 2015), from 330–190°C, and

446   from 350–210°C, respectively. The precipitation of fracture-filling chlorite occurred at

447   temperature conditions of 320°C and 340°C.

448   **Estimation of the temporal conditions of the chloritization processes.**   The temperature

449   conditions facilitating chloritization were found in the range of 180–350°C; however, the

450   formation age could not be determined due to the absence of geochronometry applicable to

451   chlorite. The temporal conditions of all the chloritization processes were determined from

452   their temperatures, using the t–T path of sample DH2 RA03 (-302.1 masl of borehole DH2)

453   within the Toki granite (Fig. S7A). Sample DH2 RA03 was obtained from a location close to

454   the sample location of this study (approximately 90 m away in horizontal distance: Fig. 1D).

455   The t–T path of sample DH2 RA03 was constructed from the thermochronological data,

456   including the ages of zircon U–Pb, biotite K–Ar, ZFT, and AFT and the FT inverse calculation

457   (Yuguchi et al., 2019B). Therefore, the weighted mean t–T path derived from the FT inverse

458   calculation was employed for this discussion. The intersection of the weighted mean t–T path

459   and the thermal condition of 350°C (blue horizontal line) give a formation age of about 68

460   Ma, and that of the t–T path and the thermal condition of 180°C give an age of about 51 Ma.

461   This indicates that all the chloritization processes had occurred over a period of about 17

462   million years from 68 to 51 Ma (Fig. S7B). The same analysis shows that the biotite,

463   hornblende, and K-feldspar chloritization processes had occurred over a period of about 17

464   million years from 68 to 51 Ma, over a period of about 10 million years from 64 to 54 Ma,

465   and over a period of 15 million years from about 68 to 53 Ma, respectively. The precipitation

466   of fracture-filling chlorite occurred at about 66 and 63 Ma.

467   **Temporal and thermal relationships of all chloritizations and plagioclase alteration.**

468   Having determined both the temporal and thermal conditions for all chloritization processes,

469   we can now discuss the sequential relationship among these processes. The temporal and

470   thermal conditions of biotite chloritization (68–51 Ma and 350–180°C) overlapped with that

471   of hornblende chloritization (64–54 Ma and 330–190°C) and K-feldspar chloritization (68–

472   53 Ma and 350–210°C), and the precipitation of fracture-filling chlorite (66 and 63 Ma, 340

473   and 320°C). In the same physical conditions of the alteration age and temperature, 1) the

474   same products occurred as chlorite regardless of the different species of reactants, and 2) the

475   precipitation of chlorite occurred within the fracture. Plagioclase alteration ages are identified

476   by illite K–Ar age of 59.2 ± 1.4 Ma (Yuguchi et al., 2019A) and K-feldspar K–Ar age of 62.2

477   ± 1.4 Ma (Yuguchi et al., in press), and the corresponding temperatures also are 305–290°C

478   and 307–325°C, respectively. The above temporal and thermal consistency indicate that the

479   serial alteration processes from all the chloritization processes to plagioclase alteration

480   process occurred within the rock body during 68–51 Ma in the temperature range of 350–

481   180°C.

482

483   **Sequential variations in the characteristics of the hydrothermal fluid**

484   **Chemical characteristics of hydrothermal fluid**.   Sequential processes from the

485   chloritizations to the plagioclase alteration occur ubiquitously in the Toki granitic rock body,

486   which impacts the fluid chemistry through hydrothermal convection throughout the pluton.

487   The ongoing reactions decrease the concentration of the inflow components and increase that

488   of the outflow components in the hydrothermal fluid. Figure 5 shows a schematic of the

489   exchange of components among the reactant, products, and hydrothermal fluid in all the

490   chloritization processes and also in the plagioclase alteration process. Chloritization reactions

491   are characterized by the following significant features: reaction with the inflow of Al^{3+}, Fe^{2+},

492   Mn^{2+}, and Mg^{2+} and the outflow of H_4SiO_4 (Si^{4+}), Ca^{2+}, K^+, and F^- (Fig. 5). Hydrogen ions

493   are observed as the reactant in biotite chloritization, whereas they are observed as the product

494   in hornblende and K-feldspar chloritizations. There is a gradual decrease in the H^+

495   concentration of the hydrothermal fluid as the biotite chloritization proceeds, indicating a

496   gradual increase in the pH of the hydrothermal fluid. Contrary to the former case, the

497   hornblende and K-feldspar chloritizations influence the gradual decrease in the pH of the

498   fluid as the alteration proceeds. The pH of the fluid gradually increases as the biotite

499   chloritization proceeds, which influenced and advanced the subsequent plagioclase alteration

500   because hydrothermal fluid with a high pH enhances the dissolution of plagioclase (Yuguchi

501   et al., 2019A). Yuguchi et al. (2019A) showed that the alteration reactions are characterized

502   by the following significant features: the inflow of H_4SiO_4 (Si^{4+}), Al^{3+}, Fe^{2+}, Mn^{2+}, Mg^{2+}, K^+,

503   and F^- and the outflow of H^+ and Ca^{2+}. The inflow components of plagioclase alteration,

504   H_4SiO_4 (Si^{4+}), K^+, and F^- correspond to the outflow components of chloritization processes

26

505   (Fig. 5). The consistency between the outflow components of chloritization and the inflow

506   components of plagioclase alteration indicates that chloritization is the dominant source of

507   mass transfer for the plagioclase alteration. That is, there is a sequence of mass transfer from

508   chloritization to plagioclase alteration.

509   The reactions of chloritization and plagioclase alteration represent the sequential

510   variations in the fluid chemistry at temporal conditions from 68 to 51 Ma as the temperature

511   cooled from 350 to 180°C. Chloritization and plagioclase alteration require the consumption

512   of aluminum, iron (ferrous), manganese, and magnesium ions (Fig. 5). Therefore, the

513   concentrations of these ions in the fluid decrease gradually as the alteration proceeds (Fig.

514   5). The alterations are accompanied with the outflow of calcium, hydrogen, and fluorine ions.

515   Thus, their concentrations in the hydrothermal fluid increase gradually as the alteration

516   proceeds (Fig. 5). The liberated calcium ions are precipitated as carbonate minerals after the

517   chloritization and plagioclase alteration (Nishimoto et al. 2008).

518   As the alteration processes progresses, a gradual increase in the concentration of

519   hydrogen ions yields a gradual decrease in pH, resulting in the termination of mineral

520   dissolution.   That is, the hornblende chloritization, K-feldspar chloritization, and

521   plagioclase alteration inhibit dissolution of reactant minerals in the hydrothermal alteration.

522   Although biotite chloritization partially produces chlorite and entirely replaces the reactant,

523   the chlorite in hornblende and K-feldspar chloritizations only partially replace the reactants,

524   which are derived from the termination of mineral dissolution due to the gradual decrease in

525   pH.

526   **Oxygen fugacity and chemistry of hydrothermal fluid.**   The hornblende-origin chlorite

27

527   in sample No. 3-2-9 involves both magnetite and ilmenite, separated by a small distance of

528   about 400 μm apart (Fig. 7A-1 and B-1).   The formation of magnetite and ilmenite are

529   associated with hornblende chloritization because their minerals are surrounded by chlorite.

530   However, the minerals were not simultaneously produced in the alteration process because

531   each mineral required a different oxygen fugacity: magnetite for high fO_2 condition and

532   ilmenite for low fO_2 condition under the same temperature. A grain of the mineral during the

533   chloritization exhibits sequential variation in its chlorite composition, representing the

534   progression of temperature conditions and chemical reactions (mass transfer) during

535   chloritization. By determining the chemical characteristics of chlorite around magnetite and

536   ilmenite, the thermal conditions of the hydrothermal fluid yielding magnetite and ilmenite

537   can be interpreted. Figure 7 shows the profiles of formation temperatures deduced from the

538   tetrahedral aluminum in the chlorite of sample No. 3-2-9: 'A area (A-1)' with scanning line

539   from 0 μm to 132 μm through ilmenite (80–115 μm) and 'B area (B-1)' with scanning line

540   from 0 μm to 84 μm through magnetite (50–65 μm). The change in chloritization temperature

541   along the scanning line in the grain indicates the extent (e.g., alteration direction) of

542   chloritization progress with temperature decrease. Area A shows a minimum temperature of

543   about 200°C, at about 50 μm in the scanning line, and the temperatures increase from there

544   to both the 0 and 132 μm sides (Fig. 7A-2). That is, the hydrothermal chloritization

545   progressed from both the sides (0 and 132 μm) and terminated at the 50-μm position in the

546   profile. Chloritization temperatures in contact with ilmenite are about 220°C (80 μm in

547   distance) and 250°C (110 μm), indicating that ilmenite was produced at temperatures

548   between 220°C and 250°C.

28

549   In area B, the chloritization temperature decreases from about 50 μm towards both sides

550   (0 and 84 μm) in the scanning line, indicating that the chloritization started at the 50-μm

551   position in the profile, and extended in both directions (Fig. 7B-2). Chloritization

552   temperatures in contact with magnetite are about 310°C (55 μm) and about 280°C (70 μm),

553   indicating that the formation temperatures of magnetite between 280 and 310°C. Therefore,

554   the formation temperature of magnetite was higher than that of ilmenite, implying a decrease

555   in oxygen fugacity in the hydrothermal fluid as temperature decreased from 280–310°C to

556   220–250°C.

557   By determining the chemical characteristics and formation temperatures of chlorite in

558   sample No. 3-2-9, the sequential variations in the fluid chemistry can be interpreted. Figure

559   8 shows the chemical variations of Al_2O_3 (A), FeO (B), MnO (C), SiO_2 (D), and MgO (E)

560   against temperature conditions of chlorite in sample No. 3-2-9. The decrease in chloritization

561   temperature is accompanied by 1) the decrease in the mass of aluminum, iron, and manganese

562   in chlorite, and 2) the increase in silicon and magnesium (Fig. 8).

563   Such profiles reflect the rates of decreasing and increasing concentrations of chemical

564   components in the hydrothermal fluid with chloritization progress, because the chemical

565   variation of chlorite corresponds to the requisite amounts of inflow and outflow components

566   in the chloritization reaction. In the trend of reduction in metallic components (aluminum,

567   iron, manganese, and magnesium ions) with the progress of hornblende chloritization

568   (overall reaction of sample No. 3-2-9: Table 2), the rates of decreasing concentrations of

569   aluminum, iron, and manganese in the hydrothermal fluid become progressively smaller,

570   while that of magnesium becomes progressively larger. The rate of increasing concentration

29

571   of silicon in the hydrothermal fluid becomes progressively smaller.

572

30

IMPLICATIONS

573

574 The methodology and interpretations for providing new insights into the mass transfer due

575 to hydrothermal alteration are described in our serial works (Yuguchi et al., 2015, 2019A,

576 and this study). They reveal the nature of the sequential, long-term variations in fluid

577 chemistry in a granitic pluton across a wide temperature range during sub-solidus cooling.

578 This study focuses on the petrography and mineral chemistry of hornblende chloritization,

579 K-feldspar chloritization, and fracture-filling chlorite formation. A combination of this study

580 and Yuguchi et al. (2015) dealing with biotite chloritization reveals the comprehensive

581 characteristics of mass transfer in the overall chloritization process, which has been either

582 overlooked or not fully appreciated in previous studies. For this study, rock samples were

583 extracted from 500-m deep boreholes. The deep drill samples enabled us to observe the

584 microvoids in hornblende chloritization. Such microstructures have not been observed

585 clearly in samples taken from the surface outcrops or from boreholes near the surface due to

586 weathering. This reveals the importance of studying deep drill samples to clarify the nature

587 of hydrothermal alteration. The SVD analysis was used to determine the chloritization

588 reaction equations, based on closure component and molar volume. This analysis can serve

589 as an effective technique to reveal the mass transfer in hydrothermal alteration and

590 metamorphic reactions with volume change. The overall reactions lead to the mass transfer

591 between the reactant and the products, and the associated inflow and outflow of components

592 with respect to the hydrothermal fluid. The time–temperature (t–T) path for the sampling site

593 is an effective tool for determining unknown alteration age from the known thermal

594 conditions of the target mineral. The sequential variations were made possible by determining

595   both the alteration age and the temperature. Determining the chemical characteristics of

596   chlorite around magnetite and ilmenite reveals that the oxygen fugacity in the hydrothermal

597   fluid during hornblende chloritization decreases as the temperature. This study, by exploring

598   the sequential variations in mass transfer and fluid chemistry, provides important procedures

599   and parameters for future forecasting the geochemical features of a granitic rock.

600

REFERENCES CITED

610

611 Alexander, W., Frieg, B., Ota, K. (2009) Grimsel Test Site Investigation Phase IV, The

612   Nagra-JAEA in situ study of safety relevant radionuclide retardation in fractured

613   crystalline rock III: The RRP project final report. Nagra Technical Report, NTB 00-07,

614   105 p.

615 Bourdelle, F., Parra, T., Chopin, C., Beyssac, O. (2013) A new chlorite geothermometer for

616   diagenetic to low-grade metamorphic conditions. Contributions to Mineralogy and

617   Petrology, 165, 723–735.

618 Carpenter, R.H., Reid, J.C., Mysers, C.W. (2017) Underground Storage of Refrigerated

619   Natural Gas in Granite of the Southeastern U.S. North Carolina Geological Survey, Open-

620   File Report 2017-02, 29 p.

621 Cathelineau, M. (1988) Cation site occupancy in chlorites and illites as a function of

622   temperature. Clay Minerals, 23, 471–485.

623 Cathelineau, M., and Nieva, D. (1985) A chlorite solid solution geothermometer. The Los

624   Azufres (Mexico) geothermal system. Contribution to Mineralogy and Petrology, 91, 235–

625   244.

626 de Caritat, P., Hutcheon, I., and Walshe, J.L. (1993) Chlorite geothermometry: A review.

627   Clays and Clay Minerals, 41, 219–239.

628 Fisher, G.W. (1989) Matrix analysis of metamorphic mineral assemblages and reactions.

629   Contributions to Mineralogy and Petrology, 102, 69–77.

630 Fisher, G.W. (1993) An improved method for algebraic analysis of metamorphic mineral

631   assemblages. American Mineralogist, 78, 1257–1261.

632   Hey, M.H. (1954) A new review of the chlorites. Mineralogical Magazine, 30, 277–292.

633   Harrison, T.M., Celerier, J., Aikman, A.B., Hermann, J., and Heizler, M.T. (2009) Diffusion

634   of ^{40}Ar in muscovite. Geochimica et Cosmochimica Acta, 73, 1039–1051.

635   Inoue, A., Inoue, S., Utada, M. (2018) Application of chlorite thermometry to estimation of

636   formation temperature and redox conditions. Clay Minerals, 53, 143–158.

637   Inoue, A., Kurokawa, K., Hatta, T. (2010) Application of chlorite geothermometry to

638   hydrothermal alteration in Toyoha geothermal system, southwestern Hokkaido, Japan.

639   Resource Geology, 60, 52–70.

640   Inoue, A., Meunier, A., Patrier-Mas, P., Rigault, C., Beaufort, D., Vieillard, P. (2009)

641   Application of chemical geothermometry to low-temperature trioctahedral chlorites.

642   Clays and Clay Minerals, 57, 371–382.

643   Ishibashi, M., Ando, T., Sasao, E., Yuguchi, T., Nishimoto, S., and Yoshida, H. (2014)

644   Characterization of water conducting fracture and their long-term behavior in deep

645   crystalline rock: A case study of the Toki granite. Journal of the Japan Society of

646   Engineering Geology, 55, 156–165 (in Japanese with English abstract).

647   Ishibashi, M., Yoshida, H., Sasao, E., and Yuguchi T. (2016) Long term behavior of

648   hydrogeological structures associated with faulting: An example from the deep crystalline

649   rock in the Mizunami URL, Central Japan. Engineering Geology, 208, 114–127.

650   Ishihara, S. (2003) Chemical contrast of the Late Cretaceous granitoids of the Sanyo and

651   Ryoke Belts, Southwest Japan: Okayama-Kagawa Transect. Bulletin of the Geological

652   Survey of Japan, 54, 95–116.

653   Ishihara, S., and Suzuki, Y. (1969) Basement granites of the Toki uranium deposits in Tono

654   region. Reports of the Geological Survey of Japan, 232, 113–127.

655   Ishihara, S., and Chappell, B. (2007) Chemical compositions of the late Cretaceous Ryoke

656   granitoids of the Chubu District, central Japan – Revisited. Bulletin of the Geological

657   Survey of Japan, 58, 323–350.

658   Ishii, T., Kogure, T., Kikuchi, R., Miyawaki, R., and Yuguchi, T. (2017). A new insight on the

659   chloritization mechanism of biotite in hydrothermally altered granite. JpGU-AGU Joint

660   Meeting 2017, SMP44-P12.

661   Itoigawa, J. (1974) Geology of the Mizunami district, central Japan. Bulletin of the Mizunami

662   Fossil Museum, 1, 9–42 (in Japanese).

663   Itoigawa, J. (1980) Geology of the Mizunami district, central Japan. Monograph of the

664   Mizunami Fossil Museum, 1, 1–50 (in Japanese).

665   Japan Nuclear Cycle Development Institute (2000) Regional Hydrogeological Study Project

666   Result from 1992–1999. JNC Technical Report, JNC TN7400 2003-007, Tono

667   Geoscience Center.

668   Japan Nuclear Cycle Development Institute (2002) Master Plan of the Mizunami

669   Underground Research Laboratory Project. JNC Technical Report. JNC TN7410 2003-

670   001, Tono Geoscience Center.

671   Jowett, E.C. (1991) Fitting iron and magnesium into the hydrothermal chlorite

672   geothermometer: GAC/MAC/SEG/ Joint Annual Meeting (Toronto, May 27–29, 1991),

673   Program with Abstract, 16, A62.

674   Kranidiotis, P., and MacLean, W.H. (1987) Systematics of chlorite alteration at the Phelps

675   Dodge massive sulfide deposit, Matagami, Quebec. Economic Geology, 82, 1898–1911.

676   Neretnieks, I. (2017) Solute transport in channel networks with radial diffusion from

677   channels in a porous rock matrix, SKB Report R-15-02, 32 p.

678   Nishimoto, S., Ukai, E., Amano, K., and Yoshida, H. (2008) Alteration process in deep

679   granitic rock - an example of Toki granite, central Japan. Journal of the Japan Society of

680   Engineering Geology, 49, 94–104 (in Japanese with English abstract).

681   Nishimoto, S., and Yoshida, H. (2010) Hydrothermal alteration of deep fractured granite:

682   Effects of dissolution and precipitation. Lithos, 115, 153–162.

683   Sano, H., Yamagata, T., and Horibo, K. (1992) Tectonostratigraphy of Mino terrane: Jurassic

684   accretionary complex of southwest Japan. Palaeogeography, Palaeoclimatology,

685   Palaeoecology, 96, 41–57.

686   Shibata, K., and Ishihara, S. (1979) Rb-Sr whole-rock and K-Ar mineral ages of granitic

687   rocks in Japan. Geochemical Journal, 13, 113–119.

688   Shigeno, M., Mori, Y., Shimada, K., and Nishiyama, T. (2012) Jadeites with metasomatic

689   zoning from the Nishisonogi metamorphic rocks, western Japan: fluid-tectonic block

690   interaction during exhumation. European Journal of Mineralogy, 24, 289–311.

691   Shikazono, N., and Kawahara, H. (1987) Compositional differences in chlorite from

692   hydrothermal altered rocks and hydrothermal ore deposits. Canadian Mineralogist, 25,

693   465–474.

694   Sonehara, T., and Harayama, S. (2007) Petrology of the Nohi Rhyolite and its related

695   granitoids: a Late Cretaceous large silicic igneous field in central Japan. Journal of

696   Volcanology and Geothermal Research, 167, 57–80.

697   Suzuki, K., and Adachi, M. (1998) Denudation history of the high T/P Ryoke metamorphic

698   belt, southwest Japan: constraints from CHIME monazite ages of gneisses and granitoids.

699   Journal of Metamorphic Geology, 16, 27–37.

700   Todo Collaborative Research Group (1999) Fault bounded inland basin of multiple blocks:

701   an example from the sedimentary basin of the Tokai Group around Tajimi City in Gifu

702   Prefecture, central Japan. Earth Science, 53, 291–306.

703   Yamasaki, S., and Umeda, K. (2012) Cooling history of the Cretaceous Toki granite in the

704   eastern Sanyo Belt, Central Japan. Japanese Magazine of Mineralogical and Petrological

705   Sciences, 41, 39–46 (in Japanese with English abstract).

706   Yoneda, T., and Maeda, H. (2008) The chemical composition of chlorites from hydrothermal

707   ore deposits and its applicability to geothermometers. Journal of MMIJ, 124, 694–699.

708   Yuguchi, T., and Nishiyama, T. (2008) The mechanism of myrmekite formation deduced

709   from steady-diffusion modeling based on petrography: Case study of the Okueyama

710   granitic body, Kyushu, Japan. Lithos, 106, 237–260.

711   Yuguchi, T., Tsuruta, T., and Nishiyama, T. (2010) Zoning of rock facies and chemical

712   composition in the Toki granitic body, Central Japan. Japanese Magazine of Mineralogical

713   and Petrological Sciences, 39, 50–70 (in Japanese with English abstract).

714   Yuguchi, T., Tsuruta, T., and Nishiyama, T. (2011A) Three-dimensional cooling pattern of a

715   granitic pluton I: The study of exsolution sub-solidus reactions in the Toki granite, Central

716   Japan. Journal of Mineralogical and Petrological Sciences, 106, 61–78.

717   Yuguchi, T., Tsuruta, T., and Nishiyama, T. (2011B) Three-dimensional cooling pattern of a

718   granitic pluton II: The study of deuteric sub-solidus reactions in the Toki granite, Central

719   Japan. Journal of Mineralogical and Petrological Sciences, 106, 130–141.

720   Yuguchi, T., Amano, K., Tsuruta, T., Danhara, T., and Nishiyama, T. (2011C)

721   Thermochronology and the three-dimensional cooling pattern of a granitic pluton: An

722   example of the Toki granite, Central Japan. Contributions to Mineralogy and Petrology,

723   162, 1063–1077.

724   Yuguchi, T., Tsuruta, T., Hama, K., and Nishiyama, T. (2013) The spatial variation of initial

725   ^{87}Sr / ^{86}Sr ratios in the Toki granite, Central Japan: Implications for the intrusion and

726   cooling processes of a granitic pluton. Journal of Mineralogical and Petrological Sciences,

727   108, 1–12.

728   Yuguchi, T., Sasao, E., Ishibashi, M., and Nishiyama, T. (2015) Hydrothermal chloritization

729   process from biotite in the Toki granite, Central Japan: Temporal variation of chemical

730   characteristics in hydrothermal fluid associated with the chloritization. American

731   Mineralogist, 100, 1134–1152.

732   Yuguchi, T., Iwano, H., Kato, T., Sakata, S., Hattori, K., Hirata, T., Sueoka, S., Danhara, T.,

733   Ishibashi, M., Sasao, E., and Nishiyama, T. (2016) Zircon growth in a granitic pluton with

734   specific mechanisms, crystallization temperatures and U-Pb ages: Implication to the

735   'spatiotemporal' formation process of the Toki granite, central Japan. Journal of

736   Mineralogical and Petrological Sciences, 111, 9–34.

737   Yuguchi, T., Sueoka, S., Iwano, H., Danhara, T., Ishibashi, M., Sasao, E., and Nishiyama, T.

738   (2017) Spatial distribution of the apatite fission-track ages in the Toki granite, central

739   Japan: Exhumation rate of a Cretaceous pluton emplaced in the East Asian continental

740   margin. Island Arc, 26, e12219 (1–15).

741   Yuguchi, T., Shoubuzawa, K., Ogita, Y., Yagi, K., Ishibashi, M., Sasao, E., and Nishiyama,

742 T. (2019A) Role of micropores, mass transfer, and reaction rate in the hydrothermal

743 alteration process of plagioclase in a granitic pluton. American Mineralogist, 104, 536–

744 556.

745 Yuguchi, T., Sueoka, S., Iwano, H., Izumino, Y., Ishibashi, M., Danhara, T., Sasao, E., Hirata,

746 T., and Nishiyama, T. (2019B) Position-by-position cooling paths within the Toki granite,

747 central Japan: Constraints and the relation with fracture population in a pluton. Journal of

748 Asian Earth Sciences, 169, 47–66.

749

750 **Appendix A**

751 **Hornblende image analysis revealing the volume (areal) ratios of the alteration minerals**

752 **obtained using image processing software, with sample No. 3-6 as an example**

753 The hornblende chloritization of sample No. 3-6 is accompanied with chlorite, titanite,

754 epidote, quartz, and calcite with microvoids and microcracks. The alteration hornblende was

755 clipped from the BSE image using the Photoshop® image processing software (Fig. S8A).

756 The binary image processing using the Photoshop® was divided into white pixels, which

757 includes hornblende and chloritization minerals (9,726,377 pixels), and black pixels (Fig.

758 S8B). These pixels corresponded to the microvoids, microcracks, and areas other than the

759 target chloritization area (9,934,423 pixels). White pixels include hornblende, chloritization

760 minerals, microvoids, and microcracks (10,286,369 pixels), while black pixels correspond to

761 areas other than the target chloritization area (9,374,431 pixels) (Fig. S8C). The chloritization

762 products consist of chlorite (3,473,645 pixels: Fig. S8D), titanite (689,597 pixels: Fig. S8E),

763 epidote (131,809 pixels: Fig. S8F), quartz (207,341 pixels: Fig. S8G), and calcite (151,928

764 pixels: Fig. S8H).

765

766 **Appendix B**

767 **Hornblende chloritization reactions of the sample No. 3-6, 7-8, 10-1 and 10-4**

768 **Sample No. 3-6: Overall reaction (Hb → Chl + Ttn + Ep + Qtz + Cal).**   Hornblende

769 (chemical composition analysis No. C3-5 in Table S1) is the reactant and chlorite (No. C3-

770 9), titanite (No. C3-1), epidote (No. C3-3), quartz (No. C3-4), and calcite (ideal $CaCO_3$ is

771 assumed) are the products. The following reaction was established by conservation involving

772 1) about 11% decrease in volume from reactant to products, and 2) volume fractions of the

773 product minerals (Chl: Ttn: Ep: Qtz: Cal = 1: 0.199: 0.038: 0.060: 0.044): Hb + $0.111Ti^+$ +

774 $3.238Al^{3+}$ + $2.066Fe^{2+}$ + $1.284Mg^{2+}$ + $0.076F^-$ + $7.039H_2O$ + $0.212CO_2$ → $0.843Chl$ +

775 $0.619Ttn$ + $0.102Ep$ + $0.473Qtz$ + $0.212Cal$ + $0.399H_4SiO_4$ + $0.015Mn^+$ + $0.916Ca^{2+}$ +

776 $0.629Na^+$ + $0.178K^+$ + $0.027Cl^-$ + $12.479H^+$ …reaction (3) (Table 2)

777   The SVD analysis of the matrices consisting of two conservation constraints of molar

778 volume and manganese components for six phases (Table S2) gives the most reasonable

779 reaction: $0.681Hb$ + $0.148Ti^+$ + $2.601Al^{3+}$ + $1.543Fe^{2+}$ + $0.820Mg^{2+}$ + $0.107F^-$ + $6.352H_2O$

780 + $0.118CO_2$ → $0.582Chl$ + $0.382Ttn$ + $0.180Ep$ + $0.073Qtz$ + $0.118Cal$ + $0.440H_4SiO_4$ +

781 $0.431Ca^{2+}$ + $0.485Na^+$ + $0.133K^+$ + $10.945H^+$ …reaction (4) (Table 2)

782 The reaction gives the volume fraction of the product minerals; Chl : Ttn : Ep : Qtz : Cal =

783 1 : 0.235 : 0.157 : 0.002 : 0.049 (Table 2).   Reaction equations (3) and (4) represent the

784 chloritization and production of titanite, epidote, quartz, and calcite by the consumption of

785 hornblende, with an inflow of Ti^+, Al^{3+}, Fe^{2+}, Mg^{2+}, F^-, H_2O, and CO_2 from the hydrothermal

786 fluid, followed by the outflow of H_4SiO_4, Mn^+ (reaction (3)), Ca^{2+}, Na^+, K^+, Cl^-, and H^+ into
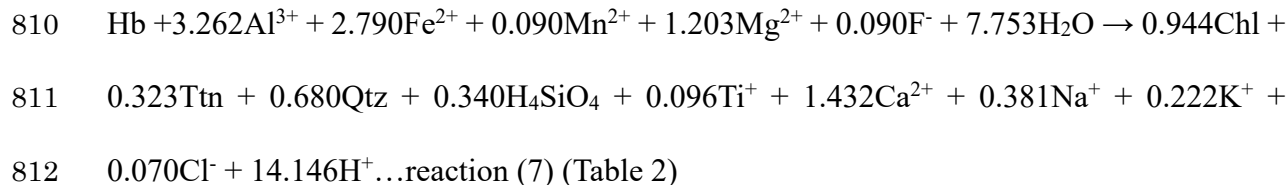
787 the hydrothermal fluid.

788   **Sample No. 7-8: Overall reaction (Hb → Chl + Ttn + Ab).**   Hornblende (No. 73) is the

789   reactant and chlorite (No. 80), titanite (No. 89), and albite (D7-1) are the products (Table S1).

790   The following reaction equation was established by conservation involving 1) about 6%

791   decrease in volume from reactant to products, and 2) volume fractions of the product minerals

792   (Chl : Ttn : Ab = 1 : 0.071 : 0.211): $Hb + 0.167H_4SiO_4 + 3.649Al^{3+} + 2.751Fe^{2+} + 0.056Mn^{2+}$

793     $+ 1.242Mg^{2+} + 6.525H_2O \rightarrow 0.933Chl + 0.253Ttn + 0.414Ab + 0.106Ti^{2+} + 1.427Ca^{2+} +$

794     $0.307Na^+ + 0.172K^+ + 0.147F^- + 0.030Cl^- + 13.719H^+$…reaction (5) (Table 2)

795   The SVD analysis of matrices consisting of two conservation constraints of molar volume

796   and Ti components for four phases (Table S2) gives the most reasonable reaction relation:

797     $0.672Hb + 0.036H_4SiO_4 + 2.541Al^{3+} + 2.192Fe^{2+} + 0.056Mn^{2+} + 0.945Mg^{2+} + 5.099H_2O \rightarrow$

798     $0.677Chl + 0.279Ttn + 0.113Ab + 0.877Ca^{2+} + 0.335Na^+ + 0.119K^+ + 0.080F^- + 0.020Cl^- +$

799     $10.341H^+$…reaction (6) (Table 2)

800   The reaction gives the volume fraction of the product minerals; Chl: Ttn: Ab = 1: 0.108:

801   0.079 (Table 2). Reactions (5) and (6) indicate that the chloritization, titanite, and albite are

802   produced by the consumption of hornblende with an inflow of H_4SiO_4, Al^{3+}, Fe^{2+}, Mn^{2+}, Mg^{2+},

803   and H_2O from the hydrothermal fluid, and are accompanied by the outflow of Ti^{2+}, Ca^{2+}, Na^+,

804   K^+, F^-, Cl^-, and H^+ into the hydrothermal fluid.

805   **Sample No. 10-1: Overall reaction (Hb → Chl + Ttn + Qtz).**   The reaction involves

806   hornblende (No. C10-5) as the reactant and chlorite (No. A096), titanite (No. E10-1), and

807   quartz (No. C10-6) as the products (Table S1). The following reaction equation was

808   established by conservations involving 1) about 12% decrease in volume from reactant to

809   products, and 2) volume fractions of the product minerals (Chl: Ttn: Qtz = 1: 0.091: 0.078):

810    $Hb +3.262Al^{3+} + 2.790Fe^{2+} + 0.090Mn^{2+} + 1.203Mg^{2+} + 0.090F^- + 7.753H_2O \rightarrow 0.944Chl +$

811    $0.323Ttn + 0.680Qtz + 0.340H_4SiO_4 + 0.096Ti^+ + 1.432Ca^{2+} + 0.381Na^+ + 0.222K^+ +$

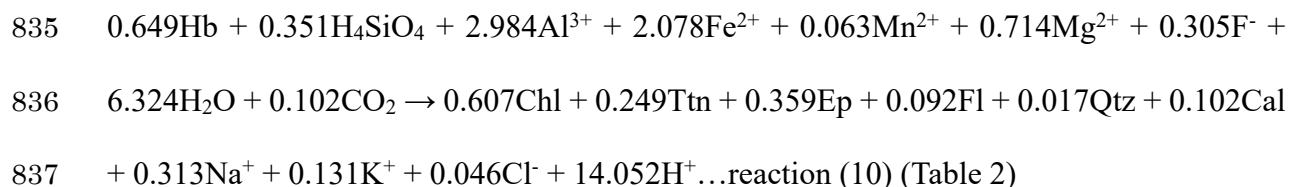812 $0.070Cl^- + 14.146H^+$…reaction (7) (Table 2)

813   The SVD analysis of the matrices consisting of two conservation constraints of molar

814   volume and Ti components for four phases (Table S2) gives the most reasonable reaction

815   relation: $0.677Hb +2.339Al^{3+} + 1.990Fe^{2+} + 0.066Mn^{2+} + 0.848Mg^{2+} + 0.091F^- + 6.288H_2O$

816    $\rightarrow 0.653Chl + 0.339Ttn + 0.025Qtz + 0.453H_4SiO_4 + 0.843Ca^{2+} + 0.258Na^+ + 0.150K^+ +$

817    $0.047Cl^- + 10.765H^+$…reaction (8) (Table 2)

818   The reaction gives the volume fraction of the product minerals; Chl : Ttn : Qtz = 1 :

819   0.138 : 0.004 (Table 2). The overall reactions are characterized by the consumption of

820   hornblende with an inflow of Al^{3+}, Fe^{2+}, Mn^{2+}, Mg^{2+}, F^-, H_2O and the production of chlorite,

821   titanite, and quartz with an outflow of H_4SiO_4, Ca^{2+}, Na^+, K^+, Cl^-, and H^+ into the

822   hydrothermal fluid.

823   **Sample No. 10-4: Overall reaction (Hb → Chl + Ttn + Ep + Fl + Cal + Qtz).**   The

824   reactant is hornblende (No. A110), and the product minerals consist of chlorite (No. A108),

825   titanite (No. C10-3), epidote (No. C10-1), fluorite (ideal CaF_2), calcite (ideal $CaCO_3$), and

826   quartz (No. E10-3). The following reaction equation was established by conservations

827   involving 1) about 11% decrease in volume from reactant to products, and 2) volume

828   fractions of the product minerals (Chl: Ttn: Ep: Fl: Cal: Qtz = 1: 0.330: 0.047: 0.094: 0.048):

829    $Hb + 1.200H_4SiO_4 + 4.487Al^{3+} + 2.740Fe^{2+} + 0.069Mn^{2+} + 0.860Mg^{2+} + 0.486Ca^{2+} + 0.730F^-$

830    $+ 7.397H_2O + 0.226CO_2 \rightarrow 0.824Chl + 0.028Ttn + 0.858Ep + 0.337Fl + 0.723Qtz +$

831    $0.226Cal + 0.199Ti^+ + 0.483Na^+ + 0.207K^+ + 0.069Cl^- + 19.592H^+$…reaction (9) (Table 2)

832   The SVD analysis of the matrices consisting of two conservation constraints of molar

833   volume and Ti and Ca components for seven phases (Table S2) gives the most reasonable

834   reaction relation:

835    $0.649Hb + 0.351H_4SiO_4 + 2.984Al^{3+} + 2.078Fe^{2+} + 0.063Mn^{2+} + 0.714Mg^{2+} + 0.305F^- +$

836    $6.324H_2O + 0.102CO_2 \rightarrow 0.607Chl + 0.249Ttn + 0.359Ep + 0.092Fl + 0.017Qtz + 0.102Cal$

837    $+ 0.313Na^+ + 0.131K^+ + 0.046Cl^- + 14.052H^+$…reaction (10) (Table 2)

838   The reaction gives the volume fraction of the product minerals; Chl : Ttn : Ep : Fl : Cal :

839   Qtz = 1 : 0.110 : 0.187 : 0.018 : 0.003 : 0.029 (Table 2). Reactions (9) and (10) indicate that

840   chlorite, titanite, epidote, fluorite, quartz, and calcite formed through the consumption of

841   hornblende with an inflow of H_4SiO_4, Al^{3+}, Fe^{2+}, Mn^{2+}, Mg^{2+}, Ca^{2+}(reaction (9)), F^-, H_2O,

842   and CO_2 from the hydrothermal fluid, followed by an outflow of Ti^+, Na^+, K^+, Cl^-, and H^+

843   into the hydrothermal fluid.

844

845   **Figure captions**

846   **Figure 1.**   The Toki granitic pluton and Mizunami Underground Research Laboratory. (A)

847   Map of Southwest Japan showing the location of the Toki granite (Tono district – TKG;

848   square symbol) in central Japan, together with the distribution of the San-in, Sanyo, and

849   Ryoke Belts in the inner zone of Southwest Japan, after Ishihara and Chappell (2007).

850   (B) Geologic map of the Toki granite after Itoigawa (1980), the Mizunami Underground

851   Research Laboratory and the borehole sites. The topographic contours inside the Tono

852   district are based on Geographical Survey Institute 1:25,000 topographic maps, titled

853   "Mitake," "Takenami," "Toki," and "Mizunami." Borehole investigations at the Toki

854   granite were performed by the Japan Atomic Energy Agency (Japan Nuclear Cycle

855   Development Institute 2000; 2002). (C) Rock facies cross-section of the Toki granite along

856   the line from X to X' on the geologic map (Fig. 1B). MBG: muscovite–biotite granite,

857   HBG: hornblende–biotite granite, and BG: biotite granite (Yuguchi et al. 2010). (D)

858   Location of the shafts and boreholes in the Mizunami Underground Research Laboratory.

859   (E) Schematic overview of the shafts in the Mizunami Underground Research Laboratory,

860   and the sample locations used in this study. The samples were collected from borehole

861   06MI03, at altitudes ranging from -274 masl (meters above sea level) to -314 masl in the

862   HBG of the Toki granite.

863   **Figure 2.**   Polarization microscope (POM) and backscattered electron (BSE) images of the

864   hornblende chloritization (A: sample No. 3-2-9, B: sample No. 7-8). The hornblende-origin

865   chlorite of sample No. 3-2-9 includes ilmenite (A-3) and magnetite (A-4). Hb: hornblende,

866   Chl: chlorite, Ab: albite, Kfs: K-feldspar, Mag: magnetite, and Il: ilmenite.

46

867   **Figure 3.**   POM and BSE images of K-feldspar chloritization (A: sample No. 3-16) and

868   fracture-filling chlorite formation (B: sample No. 8-1). The K-feldspar-origin chlorite of

869   sample No. 3-16 includes titanite and chlorite fragments and are distributed within the K-

870   feldspar grain in contact with chlorite (A-4). The fracture-filling chlorite formation is

871   accompanied by titanite and K-feldspar as the associated minerals (B-3 and B-4). Bt:

872   biotite, Chl: chlorite, Ttn: titanite, Ab: albite, and Kfs: K-feldspar.

873   **Figure 4.**   Relationship between Si (atoms per formula unit (apfu)) and Mg# (Mg / (Fe +

874   Mn + Mg) in apfu) in the overall chloritization (A), biotite chloritization (B: N = 143),

875   hornblende chloritization (C: N = 57), K-feldspar chloritization (D: N = 28), and fracture-

876   filling chlorite formation (E: N = 2). Original data of chlorite compositions in the biotite

877   chloritization were taken from Yuguchi et al. (2015).

878   **Figure 5.**   Schematic figure showing the mass transfer of chemical components through

879   hydrothermal fluids in overall chloritization and plagioclase alteration processes. Bt:

880   biotite, Hb: hornblende, Chl: chlorite, Ttn: titanite, Ep: epidote, Fl: fluorite, Cal: calcite,

881   Ab: albite, Kfs: K-feldspar, Qtz: quartz, Mag: magnetite, and Il: ilmenite.

882   **Figure 6.**   Plots of tetrahedral aluminum (Al^{IV}) in apfu (A), and formation temperature

883   deduced from Yoneda and Maeda (2008)'s geothermometer (B) among biotite

884   chloritization (N = 143), hornblende chloritization (N = 57), K-feldspar chloritization (N

885   = 28), and fracture-filling (N = 2).   Original data of chlorite compositions in the biotite

886   chloritization were taken from Yuguchi et al. (2015).

887   **Figure 7.**   Continuous thermal variation of chemical components of the hydrothermal fluid

888   associated with the formation of ilmenite (A) and magnetite (B) through the progress of

889   hornblende chloritization (sample No. 3-2-9). BSE images of the hornblende chloritization

890   associated with the formation of ilmenite (A-1) and magnetite (B-1). The profiles of

891   chloritization temperature deduced from Yoneda and Maeda (2008)'s geothermometer

892   along the scanning line: arrows in the BSE images: 0–132 μm range (A-2) and 0–84 μm

893   range (B-2). Hb: hornblende, Chl: chlorite, Ab: albite, Kfs: K-feldspar, Mag: magnetite,

894   and Il: ilmenite.

895   **Figure 8.** Variations in chemical compositions during hornblende chloritization (sample No.

896   3-2-9) with decrease in temperature: Al_2O_3 (A), FeO (B), MnO (C), SiO_2 (D), and MgO

897   (E).

898   **Supplementary figure S1.**   Chemical maps showing elemental Si, Ti, Al, Fe, Mn, Mg, Ca,

899   Na, and K concentrations in hornblende chloritization of sample No. 3-2-9 (BSE image

900   area of Fig. 2A-2). Hb: hornblende, and Qtz: quartz.

901   **Supplementary figure S2.**   POM and BSE images, and chemical maps showing elemental

902   Si, Ti, Al, Fe, Mn, Mg, Ca, Na, and K concentrations in hornblende chloritization of sample

903   No. 3-6. Hb: hornblende, Chl: chlorite, Ttn: titanite, Ep: epidote, Cal: calcite, and Qtz:

904   quartz.

905   **Supplementary figure S3.**   POM and BSE images, and chemical maps showing elemental

906   Si, Ti, Al, Fe, Mn, Mg, Ca, Na, and K concentrations in hornblende chloritization of sample

907   No. 10-1. Hb: hornblende, Chl: chlorite, and Qtz: quartz.

908   **Supplementary figure S4.**   POM and BSE images, and chemical maps showing elemental

909   Si, Ti, Al, Fe, Mn, Mg, Ca, Na, and K concentrations in hornblende chloritization of sample

910   No. 10-4. Hb: hornblende, Chl: chlorite, Ttn: titanite, Ep: epidote, Fl: fluorite, Cal: calcite,
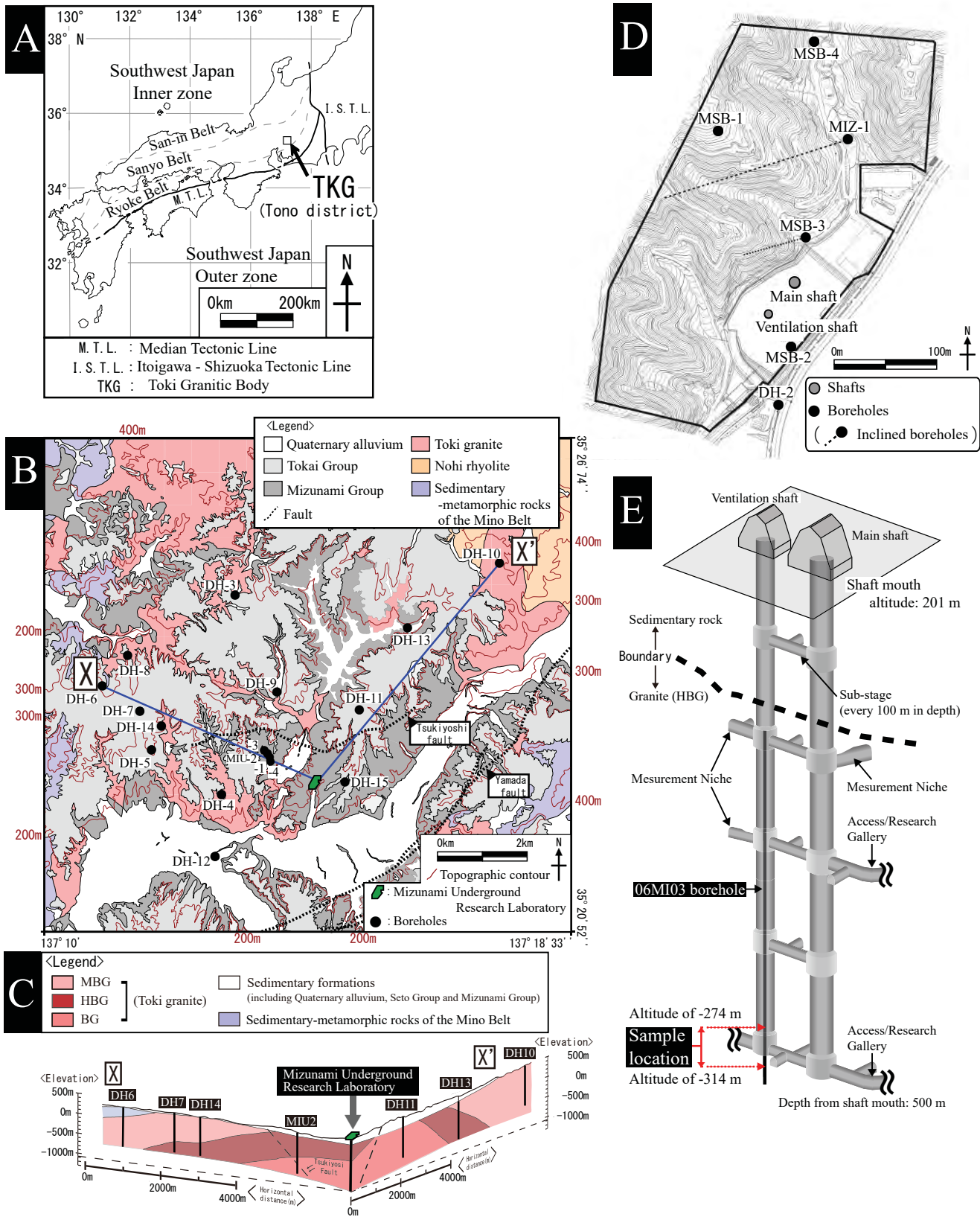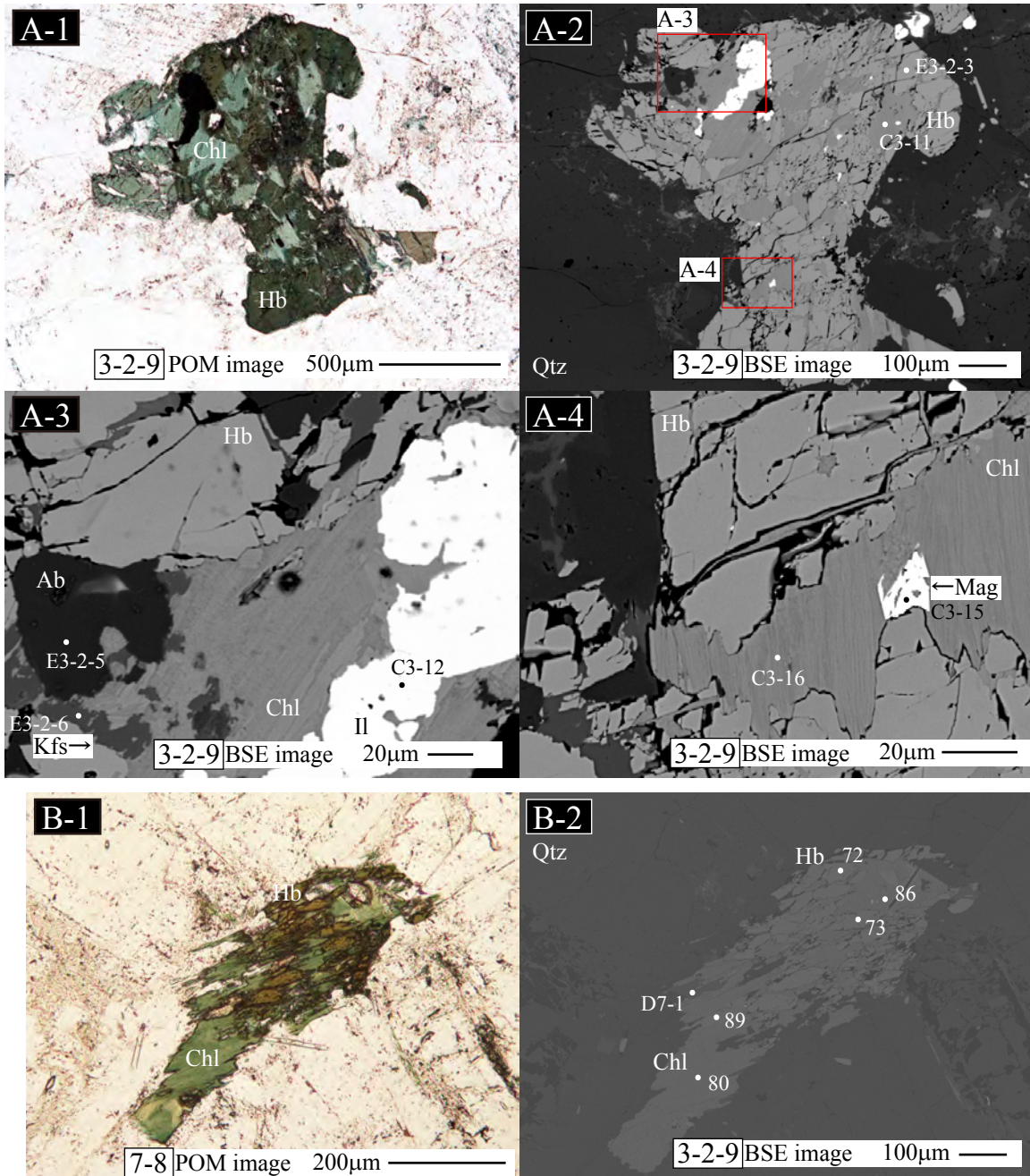
911   and Qtz: quartz.

912   **Supplementary figure S5.**   Chemical maps showing elemental Si, Ti, Al, Fe, Mn, Mg, Ca,

913   Na, and K concentrations in K-feldspar chloritization of sample No. 3-6.
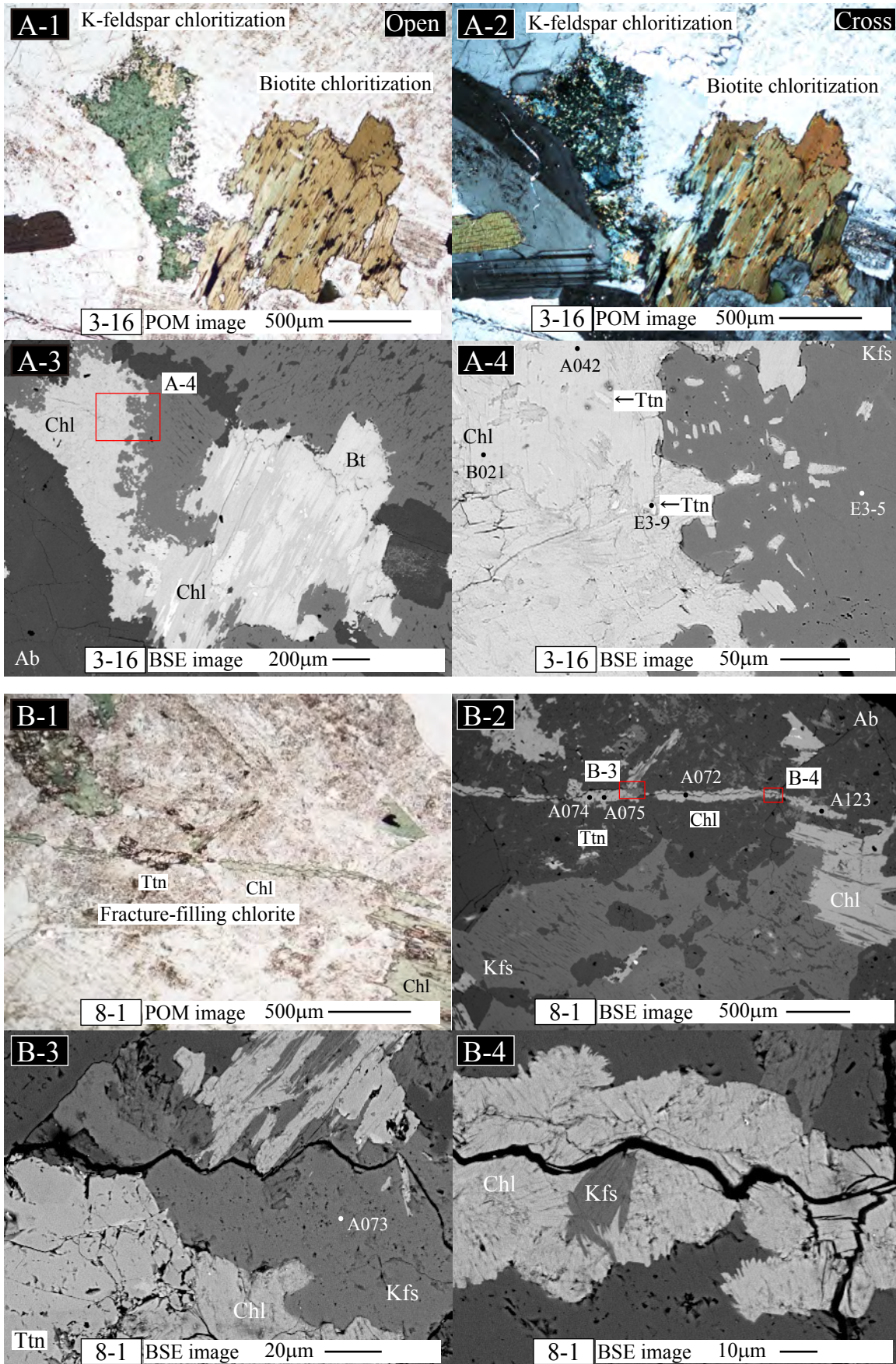
914   **Supplementary figure S6.**   Chemical maps showing elemental Si, Ti, Al, Fe, Mn, Mg, Ca,

915   Na, and K concentrations for fracture-filling chlorite of sample No. 8-1.
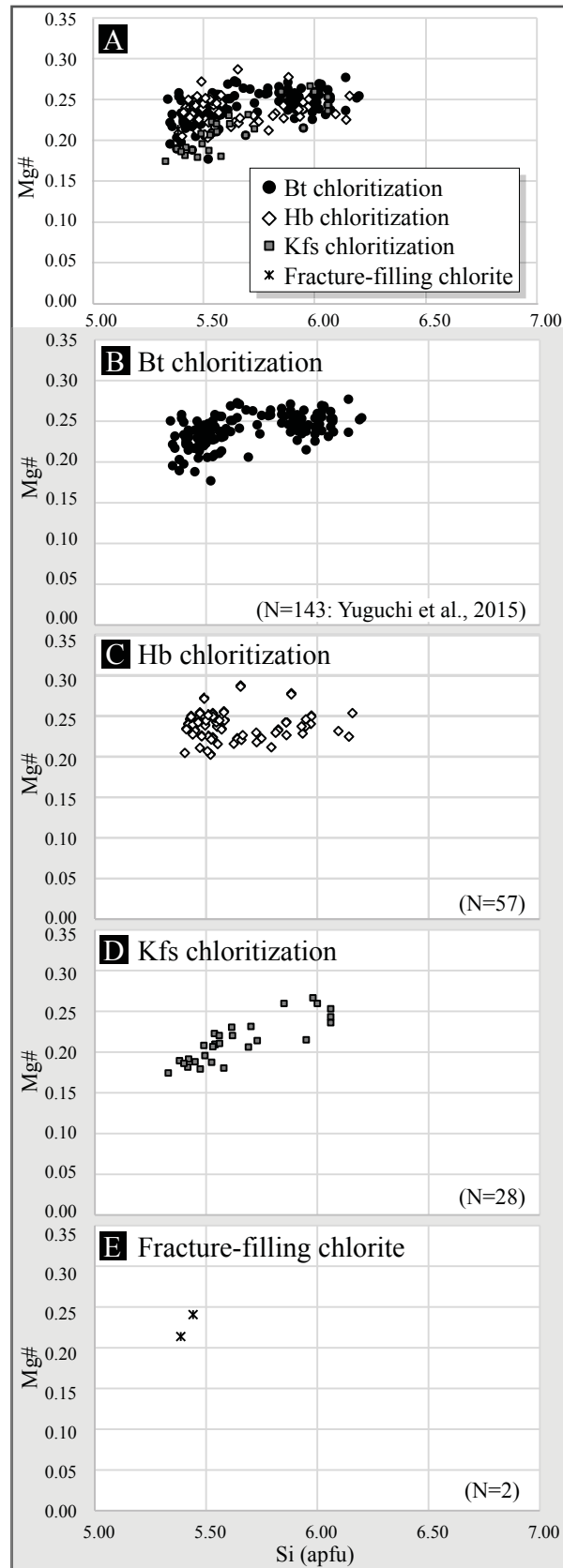
916   **Supplementary figure S7.**   The t–T path determining both the temporal and thermal

917   conditions of the secondary minerals. (A) The t–T path of sample DH2 RA03 is constructed

918   from thermochronological data including zircon U–Pb ages, biotite K–Ar age, ZFT age,

919   AFT age, and the FT inverse calculation. The FT inverse calculation was derived from a

920   dataset, including the AFT age, AFT lengths, ZFT age, and ZFT lengths, and provided the

921   acceptable-fit paths, good-fit paths, best-fit path, and the weighted mean path below 400°C.

922   The details of the FT inverse calculation are described Yuguchi et al. (2019B). The

923   envelope of good-fit paths include the biotite K–Ar, ZFT, and AFT ages, resulting in a

924   reasonable reproduction of the t–T path from the biotite K–Ar closure temperature (350–

925   400°C) through the ZFT partial annealing zone (PAZ) (190–390°C) to the AFT PAZ (60–

926   120°C). (B) The temporal condition for overall chloritization, whose thermal condition is

927   already known (Yuguchi et al., 2015 and this study), is obtained through the weighted mean

928   t–T path. In biotite chloritization, the intersection of the weighted mean t–T path and the

929   thermal condition of 350°C (blue horizontal line) gives a formation age of about 68 Ma,

930   and that of the t–T path and a thermal condition of 180°C gives an age of about 51 Ma.

931   This indicates that the biotite chloritization occurred over about 17 million years, from

932   about 68–51 Ma. The hornblende chloritization occurred at temperature conditions in the
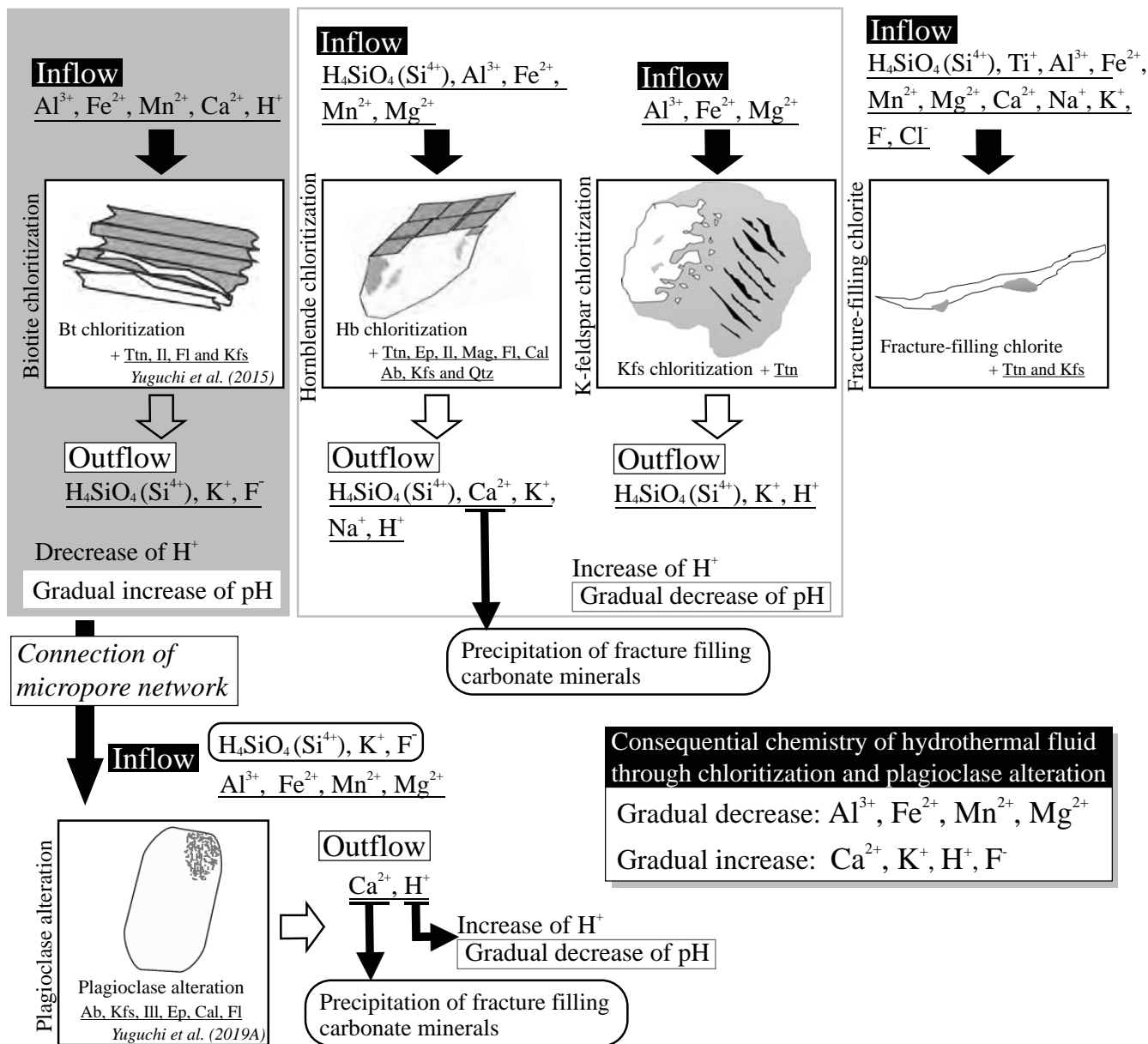
933   range of 230–325°C and over about 10 million years from about 64–54 Ma. The K-feldspar

934   chloritization occurred at temperatures in the range of 210–350°C and over about 15

935   million years of about 68 to 53 Ma. The formation conditions of fracture-filling chlorite

936   are 320°C and 340°C (thermal condition) and about 63 Ma and 66 Ma in age, respectively.

937   **Supplementary figure S8.**   Image analysis revealing the volume (areal) ratios of the

938   alteration minerals obtained using image processing software, with sample No. 3-6 as an
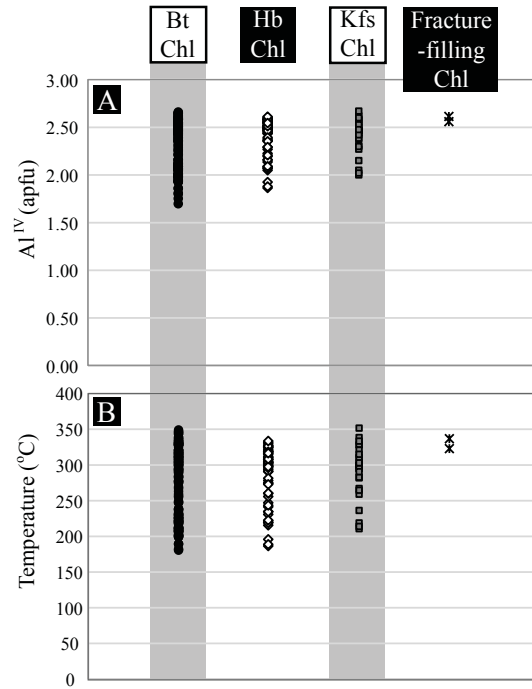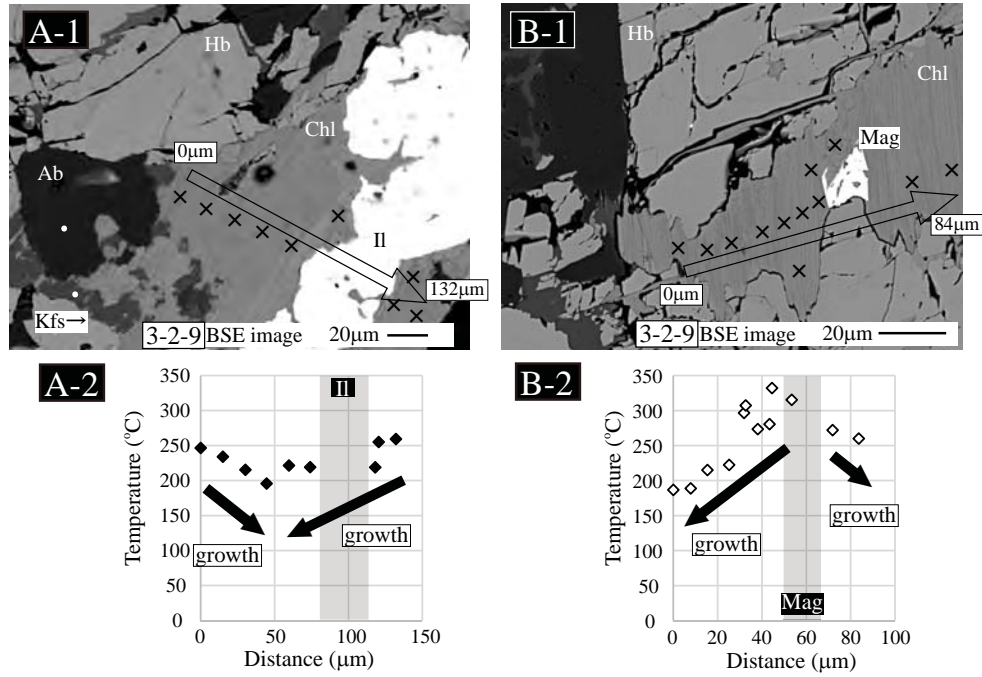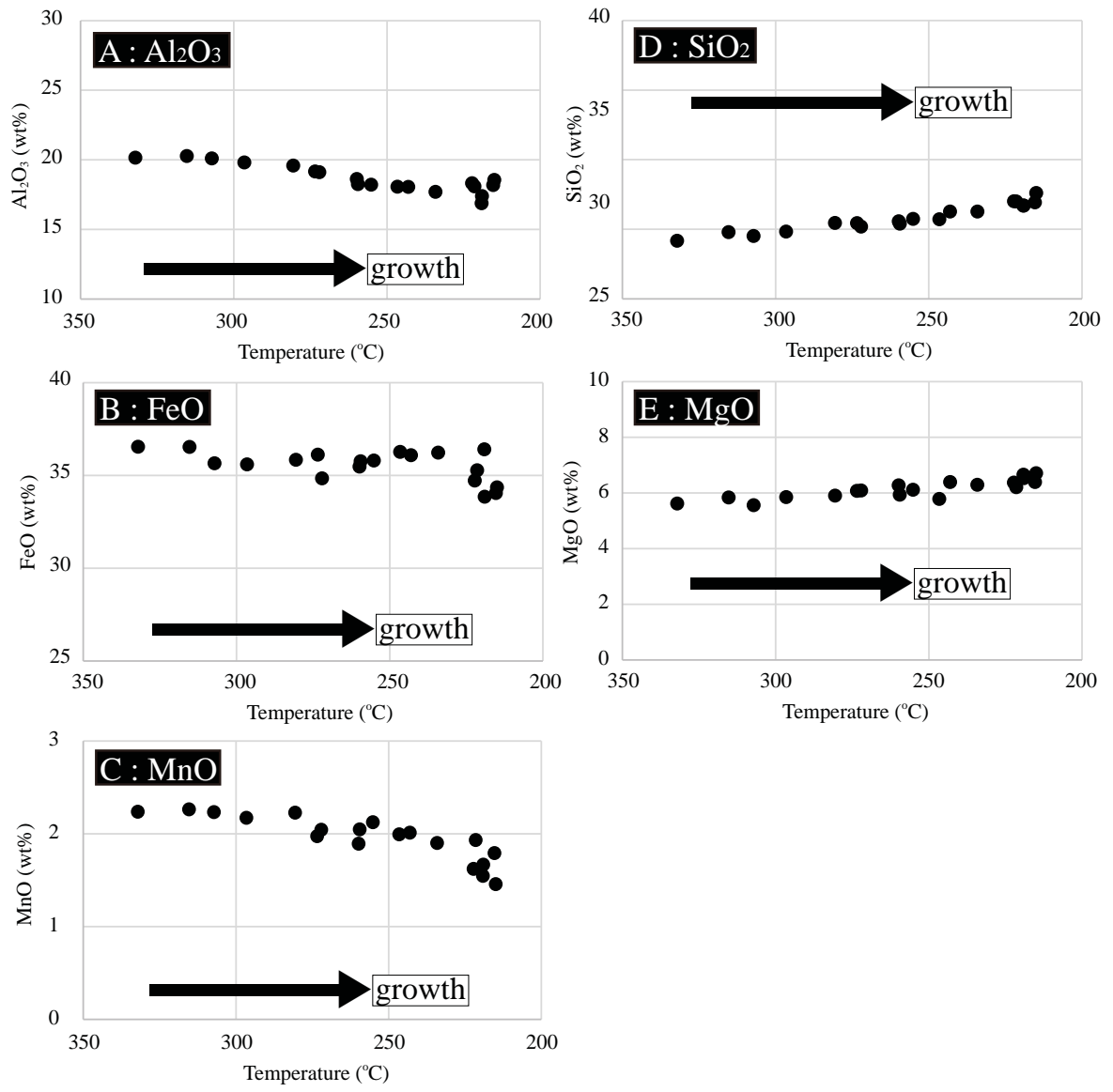
939   example.

50

Yuguchi et al. Fig. 1

Yuguchi et al. Fig. 2

Yuguchi et al. Fig. 3

Yuguchi et al. Fig. 4

Inflow
Al^{3+}, Fe^{2+}, Mn^{2+}, Ca^{2+}, H^+

Inflow
$H_4SiO_4(Si^{4+})$, Al^{3+}, Fe^{2+}, Mn^{2+}, Mg^{2+}

Inflow
Al^{3+}, Fe^{2+}, Mg^{2+}

Inflow
$H_4SiO_4(Si^{4+})$, Ti^+, Al^{3+}, Fe^{2+}, Mn^{2+}, Mg^{2+}, Ca^{2+}, Na^+, K^+, F^-, Cl^-

Biotite chloritization

Bt chloritization
+ Ttn, Il, Fl and Kfs
Yuguchi et al. (2015)

Hornblende chloritization

Hb chloritization
+ Ttn, Ep, Il, Mag, Fl, Cal Ab, Kfs and Qtz

K-feldspar chloritization

Kfs chloritization + Ttn

Fracture-filling chlorite

Fracture-filling chlorite
+ Ttn and Kfs

Outflow
$H_4SiO_4(Si^{4+})$, K^+, F^-

Drecrease of H^+
Gradual increase of pH

Outflow
$H_4SiO_4(Si^{4+})$, Ca^{2+}, K^+, Na^+, H^+

Outflow
$H_4SiO_4(Si^{4+})$, K^+, H^+

Increase of H^+
Gradual decrease of pH

Connection of micropore network

Inflow $H_4SiO_4(Si^{4+})$, K^+, F^-
Al^{3+}, Fe^{2+}, Mn^{2+}, Mg^{2+}

Precipitation of fracture filling carbonate minerals

Consequential chemistry of hydrothermal fluid through chloritization and plagioclase alteration
Gradual decrease: Al^{3+}, Fe^{2+}, Mn^{2+}, Mg^{2+}
Gradual increase: Ca^{2+}, K^+, H^+, F^-

Plagioclase alteration

Outflow
Ca^{2+}, H^+

Increase of H^+
Gradual decrease of pH

Plagioclase alteration
Ab, Kfs, Ill, Ep, Cal, Fl
Yuguchi et al. (2019A)

Precipitation of fracture filling carbonate minerals

Always consult and cite the final, published document. See http:/www.minsocam.org or GeoscienceWorld

Yuguchi et al. Fig. 6

Yuguchi et al. Fig. 7

Always consult and cite the final, published document. See http:/www.minsocam.org or GeoscienceWorld

Yuguchi et al. Fig. 8

TABLE 1. Mineral assemblage and the volume (areal) ratio of alteration minerals in the hornblende chloritization, K-feldspar chloritization, and fracture-filling chloritite.

Type [a]	Sample No.	Mineral assemblage		Volume [b] decrese (%)	Volume (areal) ratio of product minerals [d]
		Reactant	Products		
Hb chl	3-2-9	Hb	Chl, Ab, Kfs, Il, Mag	88.39	Chl : Ab : Kfs : Il : Mag = 1 : 0.056 : 0.056 : 0.131 : 0.002
Hb chl	3-6	Hb	Chl, Ttn, Ep, Qtz, Cal	89.26	Chl : Ttn : Ep : Qtz : Cal = 1: 0.199 : 0.038 : 0.060 : 0.044
Hb chl	7-8	Hb	Chl, Ttn, Ab	94.27	Chl : Ttn : Ab = 1 : 0.071 : 0.211
Hb chl	10-1	Hb	Chl, Ttn, Qtz	87.52	Chl : Ttn : Qtz = 1 : 0.091 : 0.078
Hb chl	10-4	Hb	Chl, Ttn, Ep, Fl, Cal, Qtz	89.12	Chl : Ttn : Ep : Fl : Qtz : Cal = 1 : 0.330 : 0.047 : 0.094 : 0.048
Kfs chl	3-6	Kfs	Chl, Ttn	100.00 [c]	Chl : Ttn = 1 : 0.070
Fracture chl	8-1	-	Chl, Ttn, Kfs	-	-

[a] Bt: biotite, Hb: hornblende, Chl: chlorite, Ttn: titanite, Ep: epidote, Fl: fluorite, Cal: calcite, Ab: albite, Kfs: K-feldspar, Qtz: quartz, Mag: magnetite, and Il: ilmenite.   [b] Volume decrease from reactant to products (volume percent).   [c] Constant volume from reactant to products (No decrease).   [d] The volume fraction of product minerals in the plagioclase alteration was estimated from the areal fraction of them by simply assuming the equivalence of areal and volume fractions.   The area of product minerals are identified by BSE images, and the areal ratio was calculated by image processing software of Photoshop®.

TABLE 2. Overall reactions leading to chloritization.

Sample	Overall reaction
Hb chl **Grain No. 3-2-9**	[Volume decrease of 88.39% and volume ratio of product minerals] **Hb + 0.495Ti$^+$ + 2.711Al^{3+} + 2.552Fe^{2+} + 0.265Mn^{2+} + 1.116Mg^{2+} + 0.200K$^+$ + 7.878H$_2$O** → 0.895Chl + 0.105Ab + 0.097Kfs + 0.761Il + 0.008Mag + 0.472H$_4$SiO$_4$ + 1.685Ca^{2+} + 0.500Na$^+$ + 0.131F$^-$ + 0.016Cl$^-$ + 13.870H$^+$ [**SVD**: Volume decrease of 88.39% and closure component of Ti] **0.714Hb + 2.252Al^{3+} + 1.982Fe^{2+} + 0.015Mn^{2+} + 0.825Mg^{2+} + 0.207K$^+$ + 0.022F$^-$ + 5.432H$_2$O** → 0.678Chl + 0.058Ab + 0.127Kfs + 0.098Il + 0.049Mag + 0.240H$_4$SiO$_4$ + 1.169Ca^{2+} + 0.355Na$^+$ + 0.033Cl$^-$ + 9.905H$^+$
	Volume ratio[*1] Chl : Ab : Kfs : Il : Mag = 1 : 0.400 : 0.096 : 0.022 : 0.014
Hb chl **Grain No. 3-6**	[Volume decrease of 89.26% and volume ratio of product minerals] **Hb + 0.111Ti$^+$ + 3.238Al^{3+} + 2.066Fe^{2+} + 1.284Mg^{2+} + 0.076F$^-$ + 7.039H$_2$O + 0.212CO$_2$** → 0.843Chl + 0.619Ttn + 0.102Ep + 0.473Qtz + 0.212Cal + 0.399H$_4$SiO$_4$ + 0.015Mn$^+$ + 0.916Ca^{2+} + 0.629Na$^+$ + 0.178K$^+$ + 0.027Cl$^-$ + 12.479H$^+$ [**SVD**: Volume decrease of 89.26% and closure component of Mn] **0.681Hb + 0.148Ti$^+$ + 2.601Al^{3+} + 1.543Fe^{2+} + 0.820Mg^{2+} + 0.107F$^-$ + 6.352H$_2$O + 0.118CO$_2$** → 0.582Chl + 0.382Ttn + 0.180Ep + 0.073Qtz + 0.118Cal + 0.440H$_4$SiO$_4$ + 0.431Ca^{2+} + 0.485Na$^+$ + 0.133K$^+$ + 10.945H$^+$
	Volume ratio[*1] Chl : Ttn : Ep : Qtz : Cal = 1 : 0.235 : 0.157 : 0.002 : 0.049
Hb chl **Grain No. 7-8**	[Volume decrease of 94.27% and volume ratio of product minerals] **Hb + 0.167H$_4$SiO$_4$ + 3.649Al^{3+} + 2.751Fe^{2+} + 0.056Mn^{2+} + 1.242Mg^{2+} + 6.525H$_2$O** → 0.933Chl + 0.253Ttn + 0.414Ab + 0.106Ti^{2+} + 1.427Ca^{2+} + 0.307Na$^+$ + 0.172K$^+$ + 0.147F$^-$ + 0.030Cl$^-$ + 13.719H$^+$ [**SVD**: Volume decrease of 94.27% and closure component of Ti] **0.672Hb + 0.036H$_4$SiO$_4$ + 2.541Al^{3+} + 2.192Fe^{2+} + 0.056Mn^{2+} + 0.945Mg^{2+} + 5.099H$_2$O** → 0.677Chl + 0.279Ttn + 0.113Ab + 0.877Ca^{2+} + 0.335Na$^+$ + 0.119K$^+$ + 0.080F$^-$ + 0.020Cl$^-$ + 10.341H$^+$
	Volume ratio[*1] Chl : Ttn : Ab = 1 : 0.108 : 0.079
Hb chl **Grain No. 10-1**	[Volume decrease of 87.52% and volume ratio of product minerals] **Hb +3.262Al^{3+} + 2.790Fe^{2+} + 0.090Mn^{2+} + 1.203Mg^{2+} + 0.090F$^-$ + 7.753H$_2$O** → 0.944Chl + 0.323Ttn + 0.680Qtz + 0.340H$_4$SiO$_4$ + 0.096Ti$^+$ + 1.432Ca^{2+} + 0.381Na$^+$ + 0.222K$^+$ + 0.070Cl$^-$ + 14.146H$^+$ [**SVD**: Volume decrease of 87.52% and closure component of Ti] **0.677Hb +2.339Al^{3+} + 1.990Fe^{2+} + 0.066Mn^{2+} + 0.848Mg^{2+} + 0.091F$^-$ + 6.288H$_2$O** → 0.653Chl + 0.339Ttn + 0.025Qtz + 0.453H$_4$SiO$_4$ + 0.843Ca^{2+} + 0.258Na$^+$ + 0.150K$^+$ + 0.047Cl$^-$ + 10.765H$^+$
	Volume ratio[*1] Chl : Ttn : Qtz = 1 : 0.138 : 0.004
Hb chl **Grain No. 10-4**	[Volume decrease of 89.12% and volume ratio of product minerals] **Hb + 1.200H$_4$SiO$_4$ + 4.487Al^{3+} + 2.740Fe^{2+} + 0.069Mn^{2+} + 0.860Mg^{2+} + 0.486Ca^{2+} + 0.730F$^-$ + 7.397H$_2$O + 0.226CO$_2$** → 0.824Chl + 0.028Ttn + 0.858Ep + 0.337Fl + 0.723Qtz + 0.226Cal + 0.199Ti$^+$ + 0.483Na$^+$ + 0.207K$^+$ + 0.069Cl$^-$ + 19.592H$^+$ [**SVD**: Volume decrease of 89.12% and closure components of Ti and Ca] **0.649Hb + 0.351H$_4$SiO$_4$ + 2.984Al^{3+} + 2.078Fe^{2+} + 0.063Mn^{2+} + 0.714Mg^{2+} + 0.305F$^-$ + 6.324H$_2$O + 0.102CO$_2$** → 0.607Chl + 0.249Ttn + 0.359Ep + 0.092Fl + 0.017Qtz + 0.102Cal + 0.313Na$^+$ + 0.131K$^+$ + 0.046Cl$^-$ + 14.052H$^+$
	Volume ratio[*1] Chl : Ttn : Ep : Fl : Qtz : Cal = 1 : 0.110 : 0.187 : 0.018 : 0.003 : 0.029
Kfs chl **Grain No. 3-16**	[Volume constant and volume ratio of product minerals] **Kfs + 0.107Ti$^+$ + 1.644Al^{3+} + 3.255Fe^{2+} + 0.203Mn^{2+} + 0.818Mg^{2+} + 0.113Ca^{2+} + 0.016F$^-$ + 0.009Cl$^-$ + 7.150H$_2$O** → 0.478Chl + 0.125Ttn + 0.287H$_4$SiO$_4$ + 0.016Na$^+$ + 0.911K$^+$ + 13.152H$^+$ [**SVD**: Volume constant] 0.895**Kfs + 0.051Ti$^+$ + 1.546Al^{3+} + 3.010Fe^{2+} + 0.188Mn^{2+} + 0.756Mg^{2+} + 0.050Ca^{2+} + 0.007F$^-$ + 0.009Cl$^-$ + 6.456H$_2$O** → 0.443Chl + 0.055Ttn + 0.236H$_4$SiO$_4$ + 0.014Na$^+$ + 0.814K$^+$ + 11.968H$^+$
	Volume ratio[*1] Chl : Ttn = 1 : 0.033

[*1] Volume ratio of product minerals deduced from the overall reaction